

Cite this: *Chem. Sci.*, 2025, 16, 1528

# Valorization systems based on electrocatalytic nitrate/nitrite conversion for energy supply and valuable product synthesis

Yi Feng, Jin-Tao Ren, Ming-Lei Sun and Zhong-Yong Yuan \*

The excessive accumulation of nitrate/nitrite ( $\text{NO}_x^-$ ) in surface and groundwater has severely disrupted the global nitrogen cycle and jeopardized public health. The electrochemical conversion of  $\text{NO}_x^-$  to ammonia ( $\text{NH}_3$ ) not only holds promise for ecofriendly  $\text{NO}_x^-$  removal, but also provides a green alternative to the energy-intensive Haber–Bosch process for  $\text{NH}_3$  production. Recently, in addition to the electrocatalyst design explosion in this field, many innovative valorization systems based on  $\text{NO}_x^-$ -to- $\text{NH}_3$  conversion have been developed for generating energy and expanding the range of value-added products. Collective knowledge of advanced conversion systems is indispensable for restoring the global nitrogen cycle and promoting a N-based economy. Herein, a timely and comprehensive review is provided on the important progress of valorization systems based on  $\text{NO}_x^-$  conversion, including waste treatment systems, novel electrolytic systems, and energy conversion and storage systems. Some mechanism explorations, device designs, key electrode developments and feasibility analyses are involved to gain deeper understanding of various systems and facilitate implementing these cleaning systems in industry. Finally, challenges and future prospects are outlined in the  $\text{NO}_x^-$  conversion field with an aim to promote large-scale electrocatalytic system development and prosperous N-based electrochemistry.

Received 3rd September 2024  
Accepted 28th November 2024

DOI: 10.1039/d4sc05936k

rsc.li/chemical-science

## 1. Introduction

Nitrogen is an indispensable element in the biological processes of organisms, and the global nitrogen cycle plays a crucial role in material exchange within the biosphere.<sup>1–5</sup> The severe disruption of the global nitrogen cycle is caused by the abusive use of synthetic N-containing fertilizers and chemicals,<sup>6–8</sup> causing excessive accumulation of N-species such

as nitrate/nitrite ( $\text{NO}_x^-$ ) in surface and groundwater, which may lead to eutrophic water bodies, devastated aquatic ecosystems and jeopardized public health.<sup>9</sup> For restoring the global nitrogen cycle and alleviating the pollutant effect, an electrochemistry-assisted strategy has surged as a promising approach for the degradation of  $\text{NO}_x^-$  in wastewater,<sup>10</sup> in contrast with the most widely employed conventional biotechnology method requiring an adequate organic carbon source,<sup>11</sup> which stands at the midpoint of pursuing sustainable  $\text{NO}_x^-$  removal and carbon neutrality.<sup>12–14</sup> Compared with the direct conversion to harmless and low-value  $\text{N}_2$ ,<sup>15</sup> more and more

School of Materials Science and Engineering, Smart Sensing Interdisciplinary Science Center, Nankai University, Tianjin 300350, China. E-mail: zzyuan@nankai.edu.cn



Yi Feng

Yi Feng is currently a PhD candidate under the supervision of Prof. Zhong-Yong Yuan at Nankai University. Her research interests include the rational design and synthesis of efficient electrocatalysts for electrochemical nitrate reduction and oxygen evolution reactions.



Jin-Tao Ren

Jin-Tao Ren received his PhD degree from Nankai University in 2020 under the supervision of Prof. Zhong-Yong Yuan. He is currently a postdoctoral fellow at Nankai University. His research interests focus on advanced nanomaterials for applications in electrocatalysis, metal–air batteries, fuel cells, etc.



efforts are being devoted to electrocatalytic conversion of  $\text{NO}_x^-$  to  $\text{NH}_3$  due to easier N–H bond formation and more valuable products.

$\text{NH}_3$  is a versatile chemical raw material accounting for 5% of the chemical market value and has also been acknowledged as an intriguing carbon-free energy carrier containing 17.5 wt% hydrogen ( $\text{H}_2$ ).<sup>16</sup> However, industrial synthesis of  $\text{NH}_3$  heavily relies on the Haber–Bosch process which consumes a considerable amount of energy of 5.5 EJ per year and emits about 3.0 t of  $\text{CO}_2$  per metric ton of  $\text{NH}_3$  produced.<sup>17</sup> Thus, further advancements are necessary to achieve lower temperature ammonia synthesis with a low or zero carbon footprint. So far, several attractive routes for electrocatalytic  $\text{NH}_3$  synthesis under ambient conditions have been proposed, which can be achieved by electrochemical reduction of N-containing species such as nitrogen ( $\text{N}_2$ )<sup>18</sup> and nitrogen oxides ( $\text{NO}$ ,  $\text{N}_2\text{O}$ ).<sup>19</sup> However, the electrochemical reduction efficiencies of  $\text{N}_2$ ,  $\text{NO}$  and  $\text{N}_2\text{O}$  are limited by the vigorous competition from the  $\text{H}_2$  evolution reaction (HER) due to their ultralow solubility in water (Fig. 1a and b). In contrast, electrocatalytic reduction reactions of  $\text{NO}_x^-$  are much easier to mitigate against the HER competition due to their higher solubility and more positive potentials.<sup>20</sup>

The period since 2020 has witnessed an explosive growth in the literature devoted to designing advanced electrocatalysts with high faradaic efficiency (FE) and  $\text{NH}_3$  yield rate, reflecting a comprehensive and intensive exploration of diverse electrode materials.<sup>21–23</sup> In recent years, a variety of valorization systems (Fig. 1c) based on electrochemical  $\text{NO}_x^-$ -to- $\text{NH}_3$  conversion have been developed,<sup>24–27</sup> including sewage treatment systems for  $\text{NO}_x^-$  removal and systems for producing  $\text{NH}_3$ -based chemicals, energy storage systems including metal- $\text{NO}_x^-$  batteries and  $\text{N}_2\text{H}_4$ - $\text{NO}_x^-$  batteries for energy supply and storing intermittent renewable energies, and novel electrolytic systems for production of multiple value-added chemicals. The design of novel electrolytic systems can include the modification and substitution of anode and cathode reactions. According to the cathodic reaction, integrated and tandem reactions

based on  $\text{NO}_x^-$  reduction and C species conversion can yield high-value-added chemicals such as urea<sup>28</sup> and methylamine,<sup>29</sup> which are generally synthesized through energy- and emission-intensive processes. More intriguingly, the anodic reaction is commonly the oxygen evolution reaction (OER) in an electrolyzer for electrocatalytic  $\text{NO}_3^-/\text{NO}_2^-$  reduction to  $\text{NH}_3$ , which possesses sluggish kinetics and produces low-value  $\text{O}_2$  (\$25 per ton).<sup>30</sup> Numerous reactions including oxidation of small organic molecules could then be employed to replace the anodic OER for reducing overall energy consumption and obtaining other high-value-added products.<sup>31</sup>

In view of the significance of the collective knowledge on advanced conversion systems for prosperous N-based chemistry and the scarcity of systematic reviews towards  $\text{NO}_x^-$  reduction applications, a timely and comprehensive review is provided on the recent fundamental insights and achievements of valorization systems based on  $\text{NO}_x^-$  conversion, including waste treatment systems, novel electrolytic systems, and energy conversion and storage systems. In this review, the basic knowledge of  $\text{NO}_x^-$  reduction is firstly provided including reaction mechanisms, reaction devices and design principles of catalysts. Then, the obtained technological innovations and existing challenges are elaborated on with regards to the applications of  $\text{NO}_x^-$  reduction by summarizing mechanism explorations, key electrode developments, and feasibility analyses. Finally, challenges and future prospects are outlined in the  $\text{NO}_x^-$  conversion field with an aim to promote large-scale electrocatalytic system development and prosperous N-based electrochemistry.

## 2. Fundamentals of electrocatalytic $\text{NO}_3^-/\text{NO}_2^-$ reduction

### 2.1 Reaction mechanisms

Recognizing and mastering the mechanisms of the electrocatalytic conversions of  $\text{NO}_3^-$  and  $\text{NO}_2^-$  is a prerequisite for the development of self-powered denitrification systems. Electrochemical reduction of  $\text{NO}_3^-$  is a complex process with



Ming-Lei Sun

*Ming-Lei Sun received his BE degree in 2019 from Nankai University. He is currently a PhD candidate in Nankai University under the supervision of Prof. Zhong-Yong Yuan. His research interest focuses on the fabrication of advanced nanomaterials for energy-related applications.*



Zhong-Yong Yuan

*Zhong-Yong Yuan received his PhD degree in Physical Chemistry from Nankai University in 1999. He worked as a post-doctoral fellow at the Institute of Physics, Chinese Academy of Sciences from 1999 to 2001. He then moved to Belgium, working as a research fellow at the University of Namur from 2001 to 2005, prior to joining Nankai University as a full professor. In 2016, he was elected as a fellow of the Royal Society of Chemistry (FRSC). His research interests are mainly on the self-assembly of hierarchically nanoporous and nanostructured materials for energy and environmental applications.*



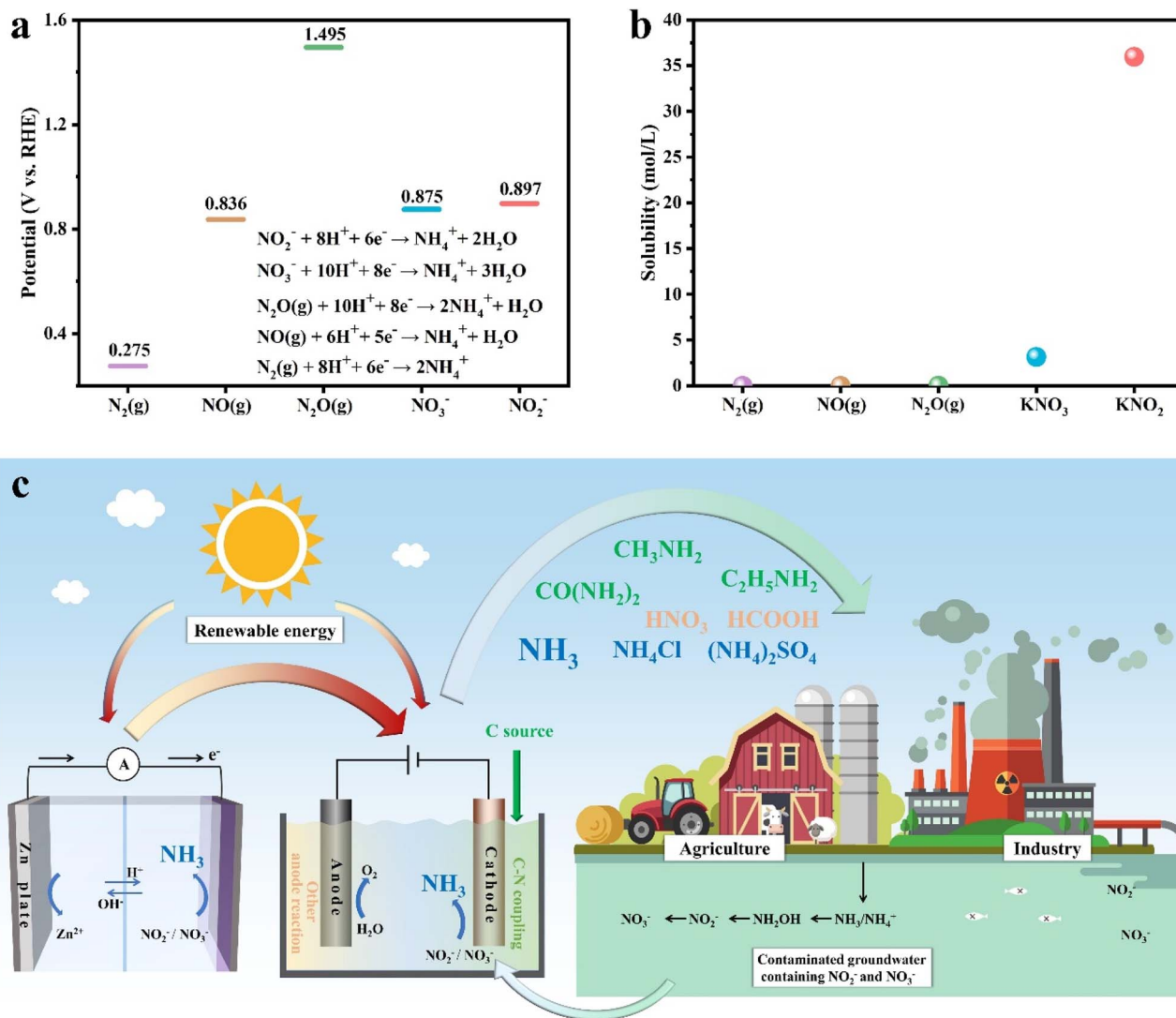


Fig. 1 (a) Theoretical potentials of the reduction reactions of  $N_2$ ,  $NO$ ,  $N_2O$ ,  $NO_3^-$  and  $NO_2^-$  to  $NH_4^+$  at the same pH (1). (b) The solubility of  $N_2$ ,  $NO$ ,  $N_2O$ ,  $KNO_3$  and  $KNO_2$  in water at room temperature. (c) The various valorization systems of electrocatalytic nitrate/nitrite conversion for energy storage and conversion, and synthesis of multiple valuable products. Red arrow: the direction of the flow of energy; green arrow: the direction of the flow of matter.

multielectron reactions,<sup>32</sup> which involves various nitrogen-containing intermediates and products ranging from  $-3$  to  $+5$  valence states.  $N_2$  and  $NH_3/NH_4^+$  are widely recognized as the most thermodynamically stable products,<sup>33</sup> but the final result can be altered due to several causes, such as cathode materials and the pH value of the solution. The indirect autocatalytic reduction mechanism and the direct electrocatalytic reduction mechanism comprise the currently accepted mechanism of  $NO_3^-$  electroreduction.<sup>34</sup> As depicted in Fig. 2, the indirect autocatalytic reaction is considered as the reduction process without  $NO_3^-$  involved in the electron transfer, only existing under the conditions of nitrate concentration exceeding 1 M and low pH value. However, more efforts are put into the mechanism of  $NO_3^-$  electroreduction occurring at concentrations lower than 1 M (direct reaction).<sup>35</sup> The active adsorbed hydrogen atom ( $H_{ads}$ )-mediated route and the electron-mediated pathway are pursued simultaneously in the direct

mechanism (Fig. 2), which leads to the complexity of the electrocatalytic  $NO_3^-$  reduction.

The electroreduction of  $NO_3^-$  is initiated by the adsorption of  $NO_3^-$  ions onto the cathodic electrodes. The adsorbed  $NO_3^-$  is transformed into  $NO_2^-$  by a tripartite electrochemical-chemical-electrochemical process, which is recognized as the dominant rate-controlling step.<sup>36</sup> Later, the nitric oxide ( $NO_{ads}$ ) intermediate is derived by  $NO_2^-$  conversion. As depicted in Fig. 2,  $NO_{ads}$  can be reduced to  $NH_3$  as the ultimate product and occupy a dominant position in the  $N_2$  formation pathway.

In addition, the reduction process of  $NO_3^-$  can be mediated by  $H_{ads}$ .  $NO_{2ads}$ ,  $NO_3^-$ , and  $NO_{ads}$  can be reduced by  $H_{ads}$ .<sup>15</sup> The predominant final product in this  $H_{ads}$ -mediated process is  $NH_3$ , which is caused by the fact that the formation of N-N bonds mediated by  $H_{ads}$  is kinetically more challenging than the formation of N-H bonds. The specific  $H_{ads}$ -mediated pathways are described by reactions (1)–(7).



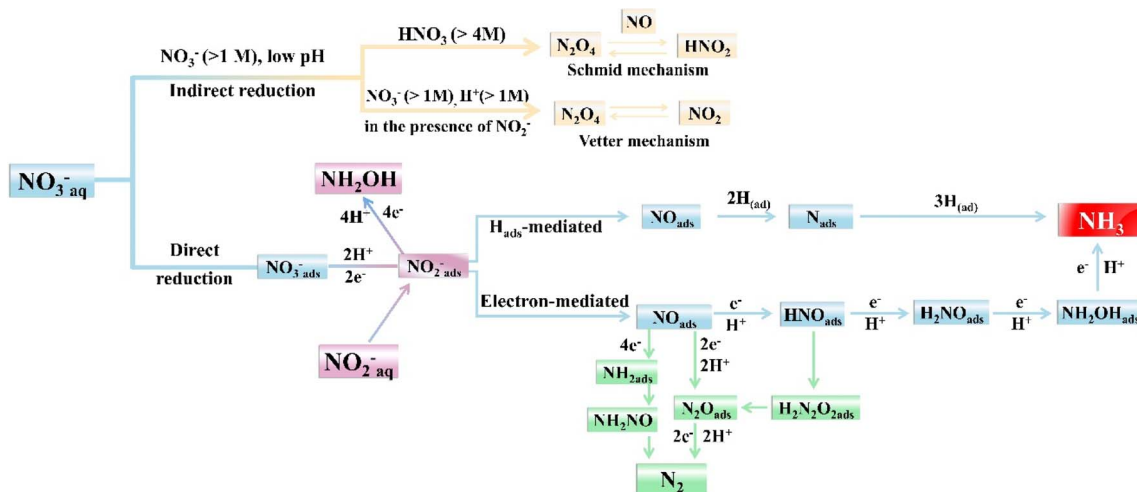
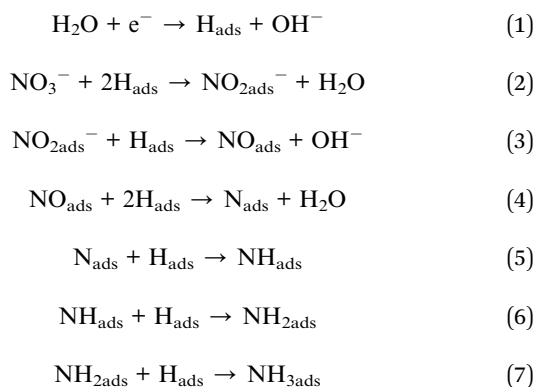
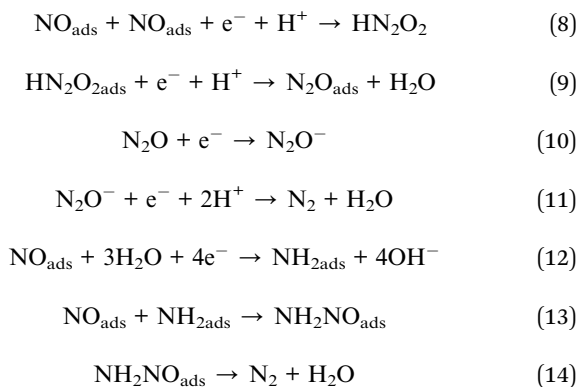


Fig. 2 Mechanisms and main processes during electrocatalytic  $\text{NO}_3^-/\text{NO}_2^-$  reduction in water.



$\text{NO}_{\text{ads}}$  is also essential for the formation of  $\text{N}_2$ . As illustrated in eqn (8)–(11), unstable  $\text{HN}_2\text{O}_2$  can be formed by  $\text{NO}_{\text{ads}}$ , sequentially forming  $\text{N}_2\text{O}_{\text{ads}}$  and  $\text{N}_2$  through electron transfer. The generation of  $\text{N}_2$  can also be obtained by the rapid decomposition of  $\text{NH}_2\text{NO}$ . It is known from eqn (12)–(14) that the stable  $\text{NH}_{2\text{ads}}$  can be formed through the  $\text{NO}_{\text{ads}}$  reduction process, which can react with  $\text{NO}_{\text{ads}}$  to form  $\text{NH}_2\text{NO}$ .



The electrocatalytic  $\text{NO}_2^-$  reduction to  $\text{NH}_3$  is roughly identical to the reduction process following the conversion of  $\text{NO}_3^-$  to  $\text{NO}_2^-$ . In fact,  $\text{NO}_2^-$  reduction is easier than  $\text{NO}_3^-$  reduction due to less charge transfer involved. In the  $\text{NO}_3^-$  reduction

process on many catalysts, the rate-limiting step is always the conversion of  $\text{NO}_3^-$  to  $\text{NO}_{2\text{ads}}^-$ .<sup>37</sup> The *in situ* Fourier transform infrared spectroscopy in most studies is employed to explore the formation of hydroxylamine ( $\text{NH}_2\text{OH}$ ) during the  $\text{NO}_2^-/\text{NO}_3^-$  reduction process, which is a vital feedstock for caprolactam synthesis and pesticide production.<sup>38</sup> However, in most cases,  $\text{NH}_2\text{OH}$  is inclined to be converted to  $\text{NH}_4^+$ .

## 2.2 Design principles of $\text{NO}_x^-$ reduction electrocatalysts

It is evident from the above that the selectivity and energy efficiency of  $\text{NO}_x^-$  reduction can be influenced by the pH of the electrolyte and the reactor designs. In general, the required potential of  $\text{NO}_x^-$  reduction in the alkaline environment is much lower than that in neutral and acidic environments.<sup>39–41</sup> Alkaline conditions are more conducive to inhibiting the competing HER compared with acidic conditions providing more active hydrogen species. In neutral or alkaline environments, the required protons for  $\text{NO}_x^-$  reduction are obtained from dissociation of water molecules. Diffusion of water molecules in neutral solutions is the rate-determining step of proton formation, while the rate-determining step in alkaline environments is the transport of adsorbed  $^*\text{OH}$ . Intriguingly, the  $^*\text{OH}$  produced facilitates the generation of  $\text{NH}_4\text{OH}$  due to the attraction of nitrogenous species, which accelerates  $\text{NO}_x^-$  reduction and reduces the competition of the HER. Thus, the design of  $\text{NO}_x^-$  reduction catalysts for alkaline conditions is discussed in the majority of efforts available currently, since  $\text{NO}_x^-$  reduction under alkaline conditions is easier to conduct with decent selectivity. In view of the neutral or acidic conditions of most wastewater, the associated design of catalysts under neutral and acidic conditions will also be discussed in the wastewater treatment section. In this section, the design principles of  $\text{NO}_x^-$  reduction catalysts under alkaline conditions will be primarily discussed.

**2.2.1 Activating N-containing intermediates.** The ideal catalyst with competitive cost is expected to exhibit high selectivity and faradaic efficiency (FE) at low potentials, resulting in



superior energy conversion efficiency and promising industrial application prospects.<sup>42</sup> The negative potentials below  $-0.2$  V are required in the majority of electrochemical systems reported for  $\text{NH}_3$  production, typically achieving unfavorable energy consumption ( $21\text{--}38 \text{ kW h kg}^{-1}$ ).<sup>43</sup> The key to reduce the overpotential and enhance the energy conversion efficiency lies in breaking the scaling relations between adsorption energy and activation energy during the reduction process.<sup>44,45</sup> The scaling relationship is proposed on the basis of Sabatier's principle, which suggests a linear relationship between the adsorption energies of certain two reaction intermediates during the heterogeneous catalytic process.<sup>46</sup> In addition, the relationship between the adsorption energy of a key intermediate and the reaction activity is exhibited in Fig. 3a. The excessively strong adsorption energy can result in catalyst surfaces that are densely covered with the intermediates, and exceedingly weak adsorption energy can prevent the reaction from proceeding.<sup>50,51</sup> Therefore, appropriate modulation of adsorption energies of reaction intermediates can facilitate the reaction by promoting the adsorption of reactants and accelerating the desorption of products. In order to obtain a better description of the scaling relationship in the  $\text{NO}_x^-$  reduction process, the activity volcano plot (Fig. 3b) has been constructed employing adsorption energies of the hollow  $^*\text{N}$  and bridge-bidentate  $^*\text{NO}_3$  as reactivity descriptors in  $\text{NO}_3^-$  reduction.<sup>48</sup> It can be observed from Fig. 3b that Cu is highly active for  $\text{NO}_3^-$  reduction and the Cu (100) facet possesses more potential to break the scaling relationship compared to the (111) facet. As described in Fig. 3c, the adsorption strength of  $^*\text{N}$  at the (100) hollow site increases with the enhancement of interatomic coupling strength ( $V_{\text{ad}}^2$ ), which is caused by the obtained dominant position of Pauli repulsion with decreasing adsorbate-metal antibonding states. The advantage of the (100) facet is displayed in Fig. 3d compared to the (111) facet, and the stronger interatomic coupling can be achieved in the (100) facet due to a shorter distance between subsurface metal-ligand and  $^*\text{N}$ . The hollow  $^*\text{N}$  is more easily destroyed due to the dominant effect of Pauli repulsion, which promotes the hydrogenation of  $^*\text{N}$  to form  $\text{NH}_3$ . This interesting strategy provides inspiration for the construction of (100)-oriented B2 CuPd nanocubes to break the scaling relationship *via* modifying the Pauli repulsion between the metallic d-state and the adsorbate frontier orbital. The (100)-oriented B2 CuPd nanocubes have been confirmed to break the scaling relationship with increased  $^*\text{NO}_3$  adsorption and attenuated  $^*\text{N}$  binding. The enhanced bridge-bidentate  $^*\text{NO}_3$  adsorption is caused by the upshift of the d-band center position in Cu after introducing Pd.

**2.2.2 Balancing nitrogen species and hydrogen species.** In addition to activation of N-containing intermediates,  $\text{H}_2\text{O}$  dissociation also deserves attention for reducing overpotential and enhancing energy efficiency. Since one  $\text{NH}_3$  requires six  $\text{H}_2\text{O}$  molecules dissociated under alkaline conditions, the  $\text{Cu}_1\text{Co}_5$  alloy is developed for  $\text{NO}_3^-$  reduction, exhibiting the higher half-cell energy efficiency of 44.9% than those of Cu, Co, and other Co-based alloys.<sup>49</sup> As demonstrated in Fig. 3e, it is suggested by the declined kinetic isotope effect in  $\text{Cu}_1\text{Co}_5$  with more favorable  $\text{NO}_3^-$  reduction activity that the bond to the

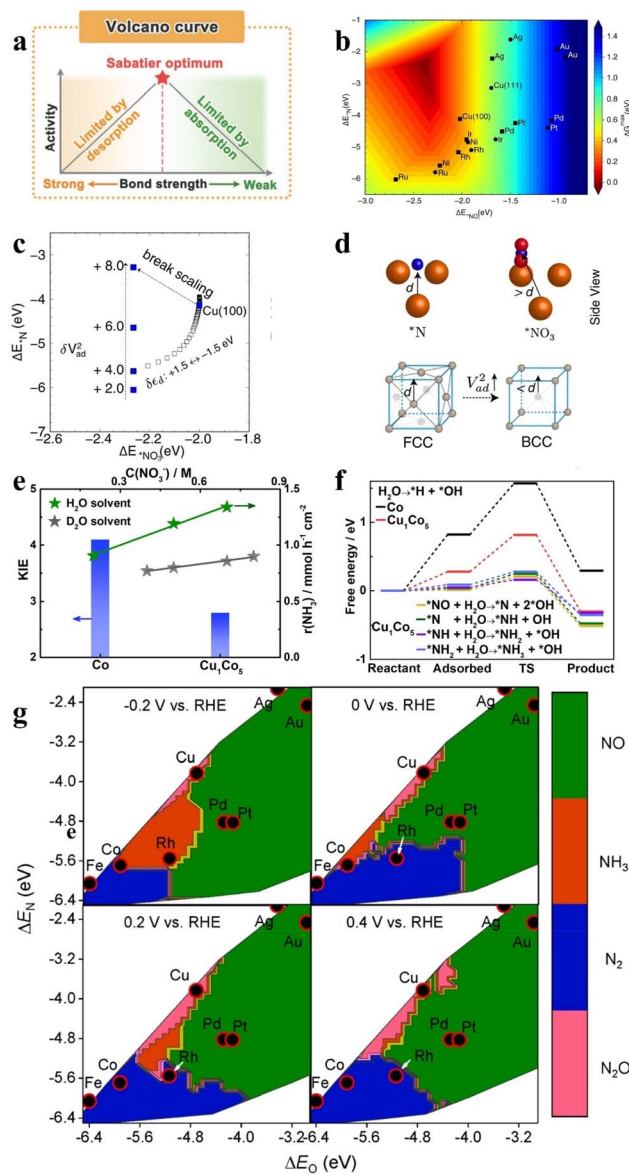


Fig. 3 (a) Volcanic curves of activity based on Sabatier's principle. Reproduced with permission.<sup>47</sup> Copyright 2022, Elsevier. (b) The activity volcano plot of various metal elements for the conversion of  $\text{NO}_3^-$  to  $\text{NH}_3$ , (c) adsorption energies of  $^*\text{NO}_3$  and  $^*\text{N}$  on Cu (100) under different  $V_{\text{ad}}^2$ . (d) The models of the (100) facet and (111) facet. Reproduced with permission.<sup>48</sup> Copyright 2022, Springer Nature. (e) Reaction kinetics and H/D kinetic isotope effect of the  $\text{NO}_3^-$  RR with  $\text{Cu}_1\text{Co}_5$  and (f) Gibbs free energies on Co and  $\text{Cu}_1\text{Co}_5$ . Reproduced with permission.<sup>49</sup> Copyright 2023, American Chemical Society. (g) Theoretical selectivity maps to various nitrogen-containing products from electrocatalytic  $\text{NO}_3^-$  reduction on the basis of  $\Delta E_{\text{O}}$  and  $\Delta E_{\text{N}}$  under different applied voltages. Reproduced with permission.<sup>33</sup> Copyright 2019, American Chemical Society.

isotopic atom is broken in the rate-determining step of  $\text{NO}_3^-$  reduction.<sup>52</sup> Fig. 3f indicates the root of remarkable activity in  $\text{Cu}_1\text{Co}_5$  under positive potentials, obtaining the beneficial dynamic equilibrium between active hydrogen generation and corresponding N-species consumption. The smaller energy barrier for  $\text{H}_2\text{O}$  adsorption on  $\text{Cu}_1\text{Co}_5$  indicates water molecules



that are more easily adsorbed and dissociated on the alloy surface. The active hydrogen formation is difficult under positive potential,<sup>53</sup> thus, H<sub>2</sub>O is directly involved in the N-species conversion process, which greatly hinders the HER side reaction.

Apart from the excellent energy conversion efficiency, high selectivity is also required in catalysts. The activity and selectivity of transition metals are exhibited in Fig. 3g for NO<sub>3</sub><sup>−</sup> reduction, which is predicted by exploring the adsorption energies of O and N atoms under different potentials.<sup>33</sup> It is revealed that catalysts with moderate ΔE<sub>O</sub> and ΔE<sub>N</sub> are inclined to exhibit more remarkable NH<sub>3</sub> selectivity at more negative potentials. The modulation of ΔE<sub>O</sub> and ΔE<sub>N</sub> can be achieved by adjusting the d-band center of the catalyst. For example, Cu50Ni50 was obtained by introducing Ni into Cu, which exhibited six-fold higher NO<sub>3</sub><sup>−</sup> reduction activity than pure Cu at the same potential.<sup>54</sup> After the introduction of Ni, the d-band center of Cu50Ni50 was shifted by 0.28 eV, compared to the d-band center position of pure Cu (−2.84 eV). The regulation of the d-band center has been confirmed to contribute to modulating the adsorption energies of intermediates including \*NO<sub>3</sub><sup>−</sup>, \*NO<sub>2</sub>, and \*NH<sub>2</sub>, leading to the enhanced performance of Cu50Ni50 for NO<sub>3</sub><sup>−</sup> reduction.

Moreover, reducing competition from other side reactions is also worthy of attention for NO<sub>3</sub><sup>−</sup> reduction in aqueous systems,<sup>55</sup> including (1) the coupling reactions between N<sub>ads</sub> and N<sub>ads</sub> for blocking NH<sub>3</sub> production and causing the generation of N<sub>2</sub>, N<sub>2</sub>H<sub>4</sub>, and N<sub>2</sub>O, (2) the competition for active hydrogen species with the HER only involving two-electron transfer. Single-atom metal-based catalysts offer new insights into reducing the direct coupling of N<sub>ads</sub> in adjacent active sites due to the lack of adjacent sites,<sup>56</sup> which is promising for inhibiting the generation of by-products including N<sub>2</sub> and N<sub>2</sub>O and enhancing NH<sub>3</sub> selectivity. In addition, the advantages of low metal loading and high metal utilization ratio in single-atom metal-based catalysts endow single-atom metal-based catalysts with the potential to be extremely cost-effective catalysts. Direct solution-phase synthesis (Fig. 4a) is employed for obtaining Cu/CuAu core/shell nanocrystals with tunable single-atom alloy layers.<sup>57</sup> The synthetic Cu/CuAu nanocrystals reach a decent FE of 85.5% in NO<sub>3</sub><sup>−</sup> reduction at −0.5 V vs. RHE with high densities of single atoms. The weakened anchoring of N<sub>ads</sub> (Fig. 4b) is conducive to the decent performance of Cu/CuAu nanocrystals, which is caused by strong repulsion from the gold ligand in subsurface or single-atom gold in the surface.

Furthermore, the NO<sub>x</sub><sup>−</sup> reduction process can be hampered by the existence of the HER, which is due to the competition for active hydrogen species<sup>60</sup> and the blockage of active sites by the H<sub>2</sub> generated.<sup>61</sup> The relatively inert metals including Cu during the water splitting process have gained much attention in numerous studies,<sup>62–64</sup> with a view to eliminating competition with the HER in NO<sub>x</sub><sup>−</sup> reduction. However, considering that the NO<sub>x</sub><sup>−</sup> reduction process relies heavily on the active hydrogen produced by H<sub>2</sub>O splitting, the blind inhibition of active hydrogen generation can hinder the subsequent hydrogenation process of the NO<sub>x</sub> reduction process. In the common design strategy, the hydrogenation process of N species is promoted by

lowering the energy barrier of \*N formation when active hydrogen is abundant. Numerous efforts have employed diverse strategies such as doping and defects to lower the energy barrier of N<sub>ads</sub> formation,<sup>65,66</sup> thus promoting the subsequent hydrogenation processes. Ni nanoparticles with grain boundary defects have been developed for opening up an entirely new strategy of utilizing water splitting and preventing H<sub>2</sub> formation.<sup>58</sup> Abundant active hydrogen species can be generated in the catalytic process due to the decent HER activity of Ni. Besides, the formation of H<sub>2</sub> is difficult on the surface owing to the strong retention capacity of active hydrogen species in grain boundary (GB) regions (Fig. 4c). With the presence of grain boundary regions, the active hydrogen species are transferred to the neighbouring adsorbed intermediates for accelerating NO<sub>x</sub><sup>−</sup> reduction. The Gibbs free energy diagrams of GB Ni for NO<sub>3</sub><sup>−</sup> reduction and the HER are exhibited in Fig. 4d and e. The excellent selectivity of GB Ni for NH<sub>3</sub> is confirmed by the lower formation energy of the N–H bond than that of N<sub>2</sub> in Fig. 4d. The stronger retention capacity of GB Ni for active hydrogen species is evidenced by the higher energy barrier for obtaining H<sub>2</sub> (Fig. 4e). In addition, the energy barrier for the conversion of \*NO<sub>3</sub> to \*NO<sub>2</sub> in the GB region is lower than that of forming H<sub>2</sub>, confirming that this strategy facilitates the inhibition of the HER, where the active hydrogen species tends to reduce \*NO<sub>3</sub> rather than form H<sub>2</sub>. The above strategy employing two sites has opened up a new avenue for achieving sufficient active hydrogen species and excellent NH<sub>3</sub> selectivity. In this strategy, the production of protons is promoted in one site acting as a proton warehouse, while the active hydrogen species are stored temporarily at the other site to facilitate subsequent hydrogenation processes.

### 2.2.3 Focusing on hydrophilic and aerophobic properties.

In addition, the hydrophilic and aerophobic properties of the catalyst surface are also deserving of emphasis.<sup>67–69</sup> In view of the blockage of NO<sub>x</sub><sup>−</sup> reduction active sites caused by the by-products including N<sub>2</sub> and H<sub>2</sub>, the ideal NO<sub>x</sub><sup>−</sup> reduction catalysts under aqueous conditions should possess strong aerophobic properties along with high affinity for aqueous electrolyte. The strongly hydrophilic surface of catalysts is more conducive to the adsorption of reactants. For example, Fe-based cyano-coordination polymer nanosheets (Fe-cyano NSs) can achieve an excellent NH<sub>3</sub> rate up to 15.49 mmol h<sup>−1</sup> cm<sup>−2</sup> with FE exceeding 90% at −0.5 V vs. RHE.<sup>59</sup> The remarkable performance can be attributed to the super-hydrophilic surface of Fe-cyano NSs (Fig. 4f), which is conducive to enhancing the contact between the electrolytes and the electrode surface for faster conversion to Fe<sup>0</sup> active sites, facilitating adsorption of NO<sub>x</sub><sup>−</sup> ions (Fig. 4g). The NO<sub>x</sub><sup>−</sup> reduction process is inevitably accompanied by side reactions producing gases such as H<sub>2</sub> and N<sub>2</sub>. Thus, enhancing the aerophobicity of the electrode interface is essential for achieving decent reaction efficiency.<sup>70</sup> As depicted in Fig. 4i, bubbles with smaller diameters are more favourable for mass transfer processes in catalysts with a stronger aerophobic nature, eliminating the accumulation of bubbles and strong adhesion on the electrode surface caused by larger bubbles.<sup>71–73</sup>



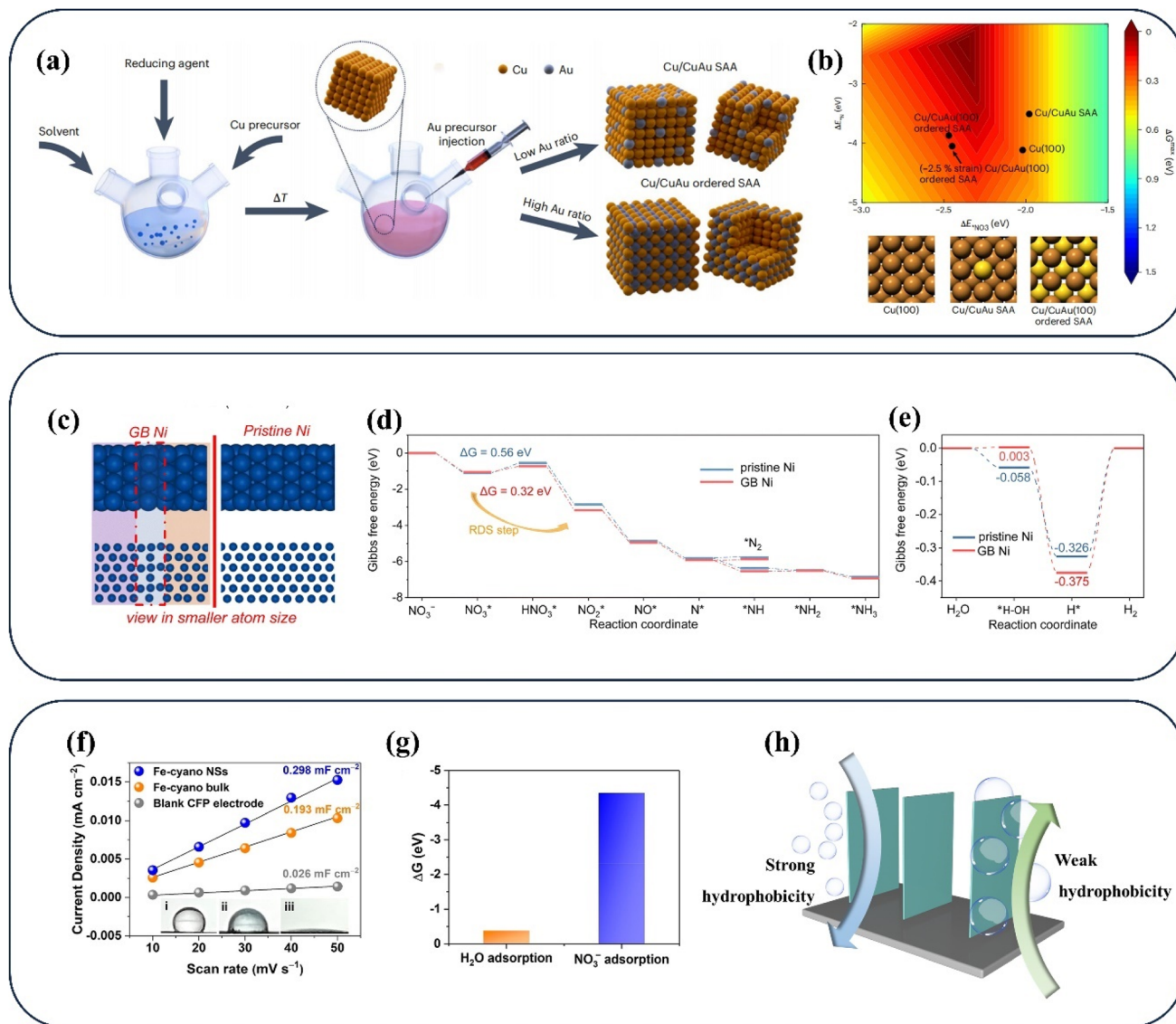


Fig. 4 (a) Schematic diagram of synthesizing Cu/CuAu core/shell nanocrystals, (b) the binding energies of  $^*\text{NO}_3$  and  $^*\text{N}$  in related catalysts. Reproduced with permission.<sup>57</sup> Copyright 2023, Springer Nature. (c) The structure model, (d) Gibbs free energy diagrams for  $\text{NO}_3^-$  reduction (e) for the HER of pristine Ni and GB Ni. Reproduced with permission.<sup>58</sup> Copyright 2023, Royal Society of Chemistry. (f) Contact angle measurement and (g) adsorption energy on Fe-cyano NSs. Reproduced with permission.<sup>59</sup> Copyright 2022, American Chemical Society. (h) The states of bubbles on different aerophobic surfaces.

It is seen above that a series of hurdles are present in  $\text{NO}_x^-$  reduction catalysts including inferior selectivity and unpromising energy conversion efficiency. In order to achieve a sustainable and competitive electrochemical ammonia production route, the following points could be considered for constructing outstanding  $\text{NO}_x^-$  reduction electrocatalysts: (1) the enhanced adsorption of  $\text{NO}_x^-$  can promote the reduction reaction, but accompanied with the dilemma of difficult product desorption. The key to solving the problem for significantly improving performance lies in breaking the scaling relationship between the adsorption energies of intermediates and reactants; (2) the competition with the HER is difficult to escape for  $\text{NO}_x^-$  reduction under aqueous conditions. Boosting  $\text{NH}_3$  selectivity and reducing  $\text{H}_2$  formation can be achieved by

employing appropriate strategies utilizing water splitting for achieving sufficient supply of active hydrogen species and hindering direct coupling of active hydrogen species; (3) the stability of intermediates including  $^*\text{NO}_{2\text{ads}}$  or  $^*\text{NOH}_{\text{ads}}$  should not be ignored for more efficient  $\text{NH}_3$  production, which can decrease other side reactions generating  $\text{N}_2$  or  $\text{NO}$ ; (4) the hydrophilic and aerophobic properties on the catalyst surface are also deserving of emphasis. The strongly hydrophilic and aerophobic surface of catalysts is more conducive to the adsorption of reactants and circumventing blocked active sites.

### 2.3 Reactor design

The current reactor designs under different scenarios are summarized in Fig. 5. The most common reaction devices



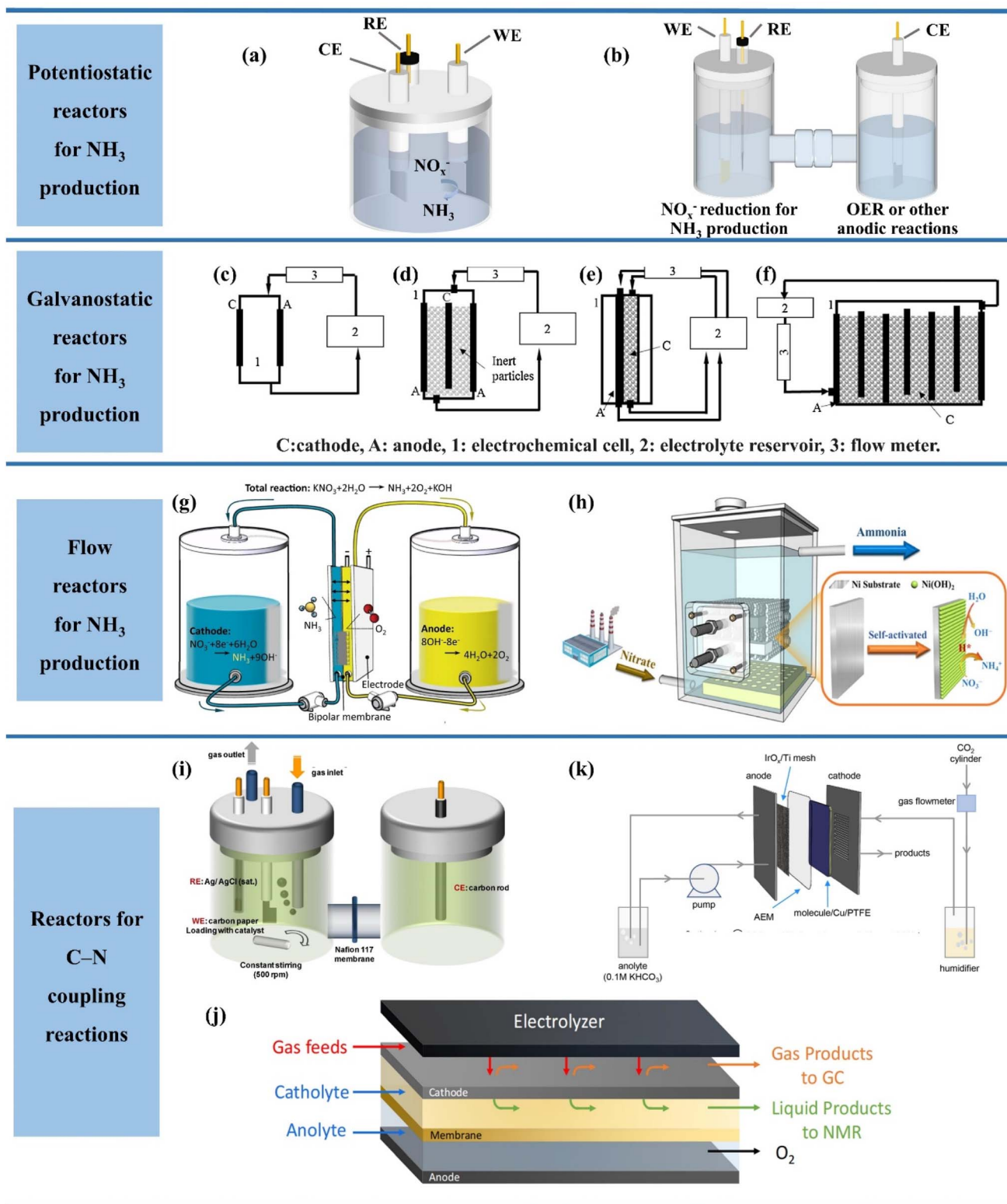


Fig. 5 (a) Single-chamber and (b) dual-chamber reactors, (c) plate electrode cell, (d) fluidizing bed of the inert particle cell, (e) packed bed cathode cell, (f) vertical moving particle bed cell. Reproduced with permission.<sup>74</sup> Copyright 2018, Elsevier. (g) Continuous NH<sub>3</sub> electrosynthesis with a bipolar membrane reactor and (h) electrochemical reactor in a pilot scale used in electrocatalytic reduction of NO<sub>3</sub><sup>-</sup>/NO<sub>2</sub><sup>-</sup>. (i) H-cells, (j) membrane-based flow reactors and (k) membrane electrode assembly electrolyzers for C–N coupling reactions. Reproduced with permission.<sup>75</sup> Copyright 2023, Elsevier.



available in the current laboratory are shown in Fig. 5a and b, which can be divided into single-chamber cells and dual-chamber cells (H-type cells). The difference between the single-chamber reactor and dual-chamber reactor is caused by the ion exchange membrane and electrode spacing. The single-chamber reactor possesses the advantages of smaller internal resistance, more simplified design and lower cost than the double-chamber reactor due to the absence of an ion exchange membrane and smaller electrode spacing.<sup>76</sup> However, it is difficult to avoid that the dissolved metal ions generated by the anode may also be deposited on the catalyst surface in a single-chamber reactor, thus reducing the FE of ammonia production.<sup>77</sup> Therefore, two chambers separated by ion exchange membranes are commonly employed in experimental studies to form a dual-chamber reactor. In spite of the higher ohmic resistance and larger energy consumption, the double chamber reactor can substantially decrease the occurrence of side reactions and enhance the FE of ammonia production. Notably, the dual-chamber reactors employed in a majority of the studies are typically operated under constant voltage. The dual-chamber reactor may not be more advantageous than a single-chamber reactor when the “multi-potential steps” are employed. For example, the *in situ* reconstruction of the Cu surface during NO<sub>3</sub><sup>-</sup> reduction was achieved by pulsed electrolysis of the Cu electrode.<sup>78</sup> Both the anodic pulsed oxidation reaction of Cu and the cathodic pulsed nitric acid reduction reaction occur in a single compartment, with the possibility of reoxidation of the reduction intermediates during the anodic pulse. In the process of electrolysis, the Cu oxidation by the anodic pulse and NO<sub>3</sub><sup>-</sup> reduction by the cathodic pulse occurred in the same chamber, where the re-oxidation of reducing intermediates may occur during the anodic pulse. In this process, the selection of single-chamber reactors is caused by the unavoidable intermediate crossover in dual-chamber cells.

Nevertheless, the reactor systems employed in experimental studies are still restricted for industrial applications. The three-electrode system (potentiostatic electrolysis) often employed in experimental studies tends to result in slower nitrate reduction owing to higher activation energy in comparison to galvanostatic electrolysis.<sup>74</sup> In addition, the struggle of the three-electrode system for large-scale application in wastewater treatment is also attributed to the complex power supply conditions.<sup>79</sup> Consequently, the galvanostatic system without the involvement of reference electrodes for control is more promising for industrial applications, but it is worth noting that the required constant applied voltage should be evaluated in advance when using galvanostatic electrolysis to suppress side reactions and maximize economic efficiency.

The designs of the reactors for galvanostatic electrolysis are displayed in Fig. 5c–f, which are more favourable for industrial applications due to the requirement of only two electrodes in the electrolyser containing the cathode and anode. The designed reactors are composed of three components, including the electrochemical cell, electrolyte reservoir and flow meter. The simplest reactor (Fig. 5c) is shown with one anode and one cathode in the electrochemical cell, which contributes to the decreased solution resistivity and reduced operating cost

due to the small spacing between the pole plate electrodes. However, the mass transfer process is not desirable enough in Fig. 5c. In order to accelerate the mass transfer, the reactor (Fig. 5d) is designed with various turbulence promoters or fluidized bed inert particles in the inter-electrode space. In addition, NO<sub>x</sub><sup>-</sup> reduction can be facilitated due to the production of reduction promoter H<sub>2</sub> when hydrogenated catalysts are employed as fluidized particles. Moreover, the further optimization of reactors is achieved in Fig. 5e and f with enhanced active area and faster mass transfer, which is caused by the packed bed cathode cells.

The reactor volume in the laboratory can hardly exceed 500 mL, which makes it extremely difficult to meet the industrial demands and achieve treating large quantities of wastewater.<sup>11</sup> In order to achieve uniform NO<sub>x</sub><sup>-</sup> reduction, the device is operated in continuous flow state. In continuous flow reactors, more challenges are imposed on electrode design, hydraulic flow state and ion-exchange membrane. The inferior hydraulic flow state can be enhanced by employing the strategies of improving reactor configuration including spiral tube reactors. Obviously, more attention is being paid to electrode design<sup>80</sup> and the improvement of the ion-exchange membrane.<sup>81</sup>

In terms of electrode design, reasonable electrode space and sufficient active sites are required to achieve accelerated mass transfer and decent reduction efficiency. Considering the technical difficulties and increased internal resistance of electrodes associated with directly enlarging the electrodes, the formation of an electrode module by multiple electrode sheets provides a reasonable solution in Fig. 5h.<sup>82</sup> The electrode module assembly is placed in a continuous flow reactor, which can overcome the drawback of insufficient reaction sites on the electrode surface and alleviate the limited treatment capacity of intermittent reactors.

In addition, ion-exchange membranes are also essential for electrochemical NH<sub>3</sub> synthesis, being required to isolate the asymmetric electrolytes on two compartments and inhibit the re-oxidation of NH<sub>3</sub> diffused to the anode. Compared with the severe ion crossover in the unipolar ion-exchange membrane, a bipolar membrane (BM) has been proposed with a mortise-tenon joint interlayer (Fig. 5g), which is composed of an anion exchange layer and a cation exchange layer.<sup>83</sup> In this modified bipolar membrane, ion selectivity is formed by electrostatic repulsion of the bipolar membrane. The total dissociation rate and the stability of the bipolar membrane are improved due to the increased hydrolysis dislocation sites. The electrolytic ammonia production device assembled with this membrane lays the foundation for the achievement of continuous and stable electrochemical ammonia synthesis at high current density exceeding 1000 mA cm<sup>-2</sup>.

As for the electrochemical C–N coupling reactions based on NO<sub>x</sub><sup>-</sup> reduction, some differences will exist in the design of the reaction equipment due to the injection of gases involved in some C–N coupling reactions. Three types of electrochemical reactors are illustrated in Fig. 5i–k demonstrating potential for application in electrochemical C–N coupling reactions, which consist of an H-type cell, membrane-based flow reactor and membrane electrode assembly (MEA) electrolyser.<sup>75</sup> The H-type



cell is the most commonly employed electrochemical reactor for C–N coupling reactions in laboratories currently due to its low cost and easy installation.<sup>84</sup> The most obvious difference between the H-type cell for C–N coupling reactions and that for  $\text{NO}_x^-$  reduction is the increase of gas inlet and outlet ports. The gaseous reactants including  $\text{CO}_2$  in the H-type cell are dissolved in aqueous solution and then diffuse to the interface between the cathode electrolyte and the working electrode. The concentration of gaseous reactants on the cathode surface is lowest due to the distance required for diffusion to the cathode in this process. In addition, the H-type cell is also still restricted for further industrial application due to its inferior mass transfer and high electrical resistance.

Membrane-based flow reactors (Fig. 5j) employing gas diffusion electrodes (GDEs) as cathodes hold promise for overcoming the drawbacks of the H-electrolyser, which possesses a continuous flow of electrolyte in both anode and cathode compartments.<sup>85</sup> Due to the presence of GDEs, the gaseous reactants can enter the cathode directly instead of diffusing from the cathode electrolyte. Consequently, the presence of GDEs ensures sufficient supply of gaseous reactants near the catalyst surface to allow the reaction to proceed at high current density. However, the membrane-based flow reactor is also hampered by poor stability, which is mainly attributed to hindered transport of gaseous reactants caused by electrolyte penetration in GDEs during the electrolysis process.

The emerging MEA electrolyzer provides novel insights into circumventing the poor stability of the membrane-based flow cell, which eliminates the cathode fluid based on the membrane-based flow cell and employs dampened reactant streams as feeding gases (Fig. 5k).<sup>86</sup> The elimination of the cathode electrolyte facilitates enhanced stability and energy efficiency of the electrochemical system, which is caused by reducing the ohmic resistance and bypassing the poor stability of GDEs due to the penetration of the electrolyte. In addition, compared to products dissolved in the electrolyte of the membrane-based flow cell, products obtained by the MEA electrolyser remain in the gaseous phase, which is easy to collect by condensation for dramatically reducing the cost of separating the product. In spite of the unexplored application of the MEA electrolyser in C–N coupling reactions currently, it has provided a promising approach to achieve ultrastable C–N coupling reactions at high current density.

### 3. Wastewater treatment

Enormous efforts have been made towards the removal of  $\text{NO}_3^-/\text{NO}_2^-$  in underground water for restoring the global nitrogen cycle. Public health is directly threatened by  $\text{NO}_x^-$  ions which impair oxygen transport and trigger the “blue baby syndrome”. More importantly, the destroyed ozone layer and worsened global warming can be caused by  $\text{N}_2\text{O}$  generated through bacterial denitrification in nature.<sup>87</sup> The electrochemical  $\text{NO}_x^-$  reduction has gained much attention as a promising denitrification alternative, which possesses the advantages of mild operating conditions, no deleterious residues and small installation footprint. Although the  $\text{NO}_x^-$

reduction to  $\text{NH}_3$  pathway has demonstrated more benefits than  $\text{NO}_x^-$  reduction to  $\text{N}_2$  owing to the easier formation of the N–H bond and higher application value of  $\text{NH}_3$ , it is worth noting that employing the  $\text{NO}_x^-$ – $\text{NH}_3$  approach for treating wastewater has also been doubted due to the following two reasons: (1) the uncompetitive economic benefits due to insufficient  $\text{NO}_x^-$  concentration;<sup>88</sup> (2) the difficult extraction of dissolved  $\text{NH}_3$  causing worse environmental implications.<sup>89</sup> Thus, the treatment of wastewater containing nitrate/nitrite is recommended in many efforts to convert low-concentration  $\text{NO}_x^-$  ions into  $\text{N}_2$  or recycle high-concentration  $\text{NO}_x^-$  ions to other N-containing fertilizers.<sup>90–92</sup> For achieving the optimal balance between efficiency and economy in large-scale wastewater treatment employing the  $\text{NO}_x^-$ – $\text{NH}_3$  approach, it is necessary to delve into electrocatalyst development, actual wastewater composition, reaction system design and product separation.

#### 3.1 Factors influencing electrochemical $\text{NO}_x^-$ reduction

In view of the complex composition of wastewater, several studies have explored the influences of ion concentration, other existing inorganic ions, and pH on  $\text{NO}_x^-$  reduction in wastewater to facilitate more efficient utilization of wastewater streams for ammonia production.<sup>93–95</sup> The concentrations and species of ions in some common wastewater sources are illustrated in Table 1. Indeed,  $\text{NO}_2^-$  reduction to  $\text{NH}_3$  is thermodynamically and kinetically facile, making it promising for  $\text{NH}_3$  synthesis. Despite the mass of  $\text{NO}_2^-$  in wastewaters is far less than that of  $\text{NO}_3^-$  (Table 1),  $\text{NO}_3^-$  ions in wastewater are always transformed to  $\text{NO}_2^-$  by micro-organisms. With respect to the effects of other ions, it is obvious that  $\text{NO}_3^-$  in sufficiently large concentrations is far more competitive than other ions, and thus the reaction rate is hardly affected.<sup>100</sup> However, such wastewater is not especially common and therefore concentrated  $\text{NO}_3^-$ -containing wastewater offers greater potential for ammonia production. The effects of pH and other inorganic ions on the reaction rate of the nitrate reduction process should not be neglected. The  $\text{NO}_x^-$  reduction reaction can be conducted over a broad range of pH; however, the performance and selectivity of  $\text{NO}_x^-$  reduction differ dramatically at different pH conditions. In addition, the drastic changes in the pH of the electrode interface and solution probably cause altered reaction mechanisms during the reduction process with proton depletion or ammonium hydroxide production.<sup>101</sup> Thus, buffer solutions with high concentrations are employed to mitigate drastic changes of pH in the majority of studies on electrochemical  $\text{NO}_x^-$  removal. The dominant HER under acidic conditions can diminish the selectivity and FE of  $\text{NO}_x^-$  reduction. Despite the fact that the selectivity of  $\text{NO}_x^-$  reduction can be enhanced under alkaline conditions, the reduction kinetics can be boosted with the presence of indirect catalytic processes in acidic environment. It has been confirmed that  $\text{NO}_2^-$  is the dominant product for  $\text{NO}_3^-$  reduction in an alkaline environment, and the generation of  $\text{NH}_3$  can be accelerated with the increase of proton concentration.<sup>11</sup>

For inorganic ions, the impacts on nitrate reactions are diverse, including positive and negative effects. It is found that



Table 1 Available  $\text{NO}_3^-/\text{NO}_2^-$ -rich wastewater streams

Type of wastewater	pH	Main composition	$\text{NO}_3^-$ concentration	$\text{NO}_2^-$ concentration	Ref.
Textile wastewater	Neutral	$\text{NO}_3^-$ , $\text{Cl}^-$	7.4 mM	—	96
Industrial wastewater	Alkalescent	$\text{NO}_3^-$ , $\text{NH}_4^+$ , $\text{Cl}^-$	41.6 mM	—	97
Polluted ground water	Unknown	$\text{NO}_3^-$ , $\text{NO}_2^-$ , $\text{NH}_4^+$	0.88–1.26 mM	0.22–1.27 mM	98
Low-level nuclear wastewater	Alkaline	$\text{NO}_3^-$ , $\text{NO}_2^-$ , $\text{SO}_4^{2-}$ , $\text{CO}_3^{2-}$ , $\text{Cl}^-$ , $\text{F}^-$ , $\text{SiO}_3^{2-}$ , $\text{CrO}_4^{2-}$	1.95 M	0.55 M	99

alkali metal cations follow the order of  $\text{Li}^+ < \text{Na}^+ < \text{K}^+ < \text{Cs}^+$  to enhance the rate of  $\text{NO}_3^-$  reduction.<sup>11</sup> The cations weaken the repulsive force between the negative ions and the cathode and facilitate the reduction of  $\text{NO}_3^-$  on the cathode since the cations modify the bimolecular structure of the cathode and form transient neutral ion pairs.<sup>102</sup> As for multivalent cations, the presence of  $\text{NH}_4^+$ ,  $\text{Ca}^{2+}$  and  $\text{La}^{3+}$  can achieve higher rates than alkali metal cations, but some cations such as  $\text{Ca}^{2+}$  and  $\text{Mg}^{2+}$  can be adsorbed on the cathode surface to form precipitates, resulting in poisoning of the cathode active sites and reduced reaction rates.<sup>103</sup> Similarly, the reduction reaction of  $\text{NO}_3^-$  is also affected by anions. The negative effect of anions on the reaction rate is caused by the competition of anions for adsorption sites. The anions are ranked in the order of  $\text{I}^- > \text{Br}^- > \text{Cl}^- > \text{F}^-$  to reduce the rate of nitrate reduction.<sup>104</sup>

### 3.2 Reactors for $\text{NO}_x^-$ removal and product collection

The continuous flow state is usually adopted in the operation of industrialized reactors. In spite of the preliminary discussion of continuous flow reactors in Section 2.2, the feasibility of reactors is of significant importance for enhancing the scale and commercial value of wastewater treatment.<sup>105</sup> Regrettably, the feasibility of continuous flow reactors has rarely been explored for removing  $\text{NO}_x^-$  ions in current studies. Makover *et al.* have explored the feasibility of Cu-dimensionally stable anode (DSA) electrodes in a continuous flow reactor (Fig. 6a) for treating sewage after Donnan dialysis.<sup>106</sup> The anode (DSA) employed is Ti covered with  $\text{RuO}_2/\text{IrO}_2$ . In Donnan dialysis, the  $\text{NO}_x^-$  ions in sewage will transfer to the receiver compartment from the feed compartment due to electroneutrality induction, accompanied with the transfer of high concentration  $\text{Cl}^-$  and  $\text{SO}_4^{2-}$  ions into the receiver driven by a concentration gradient. The excellent results employing Cu-DSA electrodes are obtained in high salinity  $\text{NO}_x^-$  contaminated solution generated by Donnan dialysis. Optimal  $\text{NO}_3^-$  removal can be reached at a low current density of  $10 \text{ mA cm}^{-2}$  and short residence time of 90 min, reaching 63% in high salinity  $\text{Na}_2\text{SO}_4$  and 44% in high salinity  $\text{NaCl}$ . The promotion effect of high salinity  $\text{SO}_4^{2-}$  ions and the inhibition effect of high salinity  $\text{Cl}^-$  ions on nitrate removal have also been confirmed.

In the current studies of separating products, converting  $\text{NH}_3$  to  $(\text{NH}_4)_2\text{SO}_4$  by coupling acid adsorption is a reasonable route. Fig. 6b exhibits a three-chamber membrane distillation reactor by coupling electrocatalysis with acid absorption.<sup>5</sup> The electrodes involved in Fig. 6b are generally self-supported electrodes with active sites that fail to be fully utilized, compared with the homogeneous molecular catalyst achieving

precise atomic coordination between reactants and catalytic active sites. Thus, a series of electrochemical stripping (ECS) reactors are developed using homogeneous molecular catalyst Co(DIM) for degrading contaminants and extracting products in large-volume and nitrate-rich wastewaters (typically  $< 4 \text{ mM}$ ).<sup>107</sup> The ECS recirculating batch process is shown in Fig. 6c. A cation exchange membrane (CEM) is used to avoid  $\text{NO}_x^-$  diffusion from the cathode chamber to the anode compartment. During the reduction process, the increased pH of the catholyte is expected to exceed the  $\text{pK}_a$  of  $\text{NH}_3$  (9.25), causing the majority of products to be in the form of volatile  $\text{NH}_3$ . Thus, a hydrophobic breathable membrane is utilized for dispersing volatile  $\text{NH}_3$  from the cathode chamber. The operation for 42 h in this reactor witnessed 70.5%  $\text{NO}_x^-$  removal, which makes the treated water meet the drinking water limit. Moreover, the  $\text{NH}_3$  selectivity remains over 98.5% throughout this period which confirms that the Co(DIM)-mediated  $\text{NO}_x^-$  reduction is rarely influenced by wastewater constituents.

In order to reduce electrical energy consumption and enhance the ammonia recovery rate, two additional process configurations are explored in Fig. 6d and e. In a parallel feed configuration (Fig. 6d), the  $\text{KClO}_4$  solution is replaced by  $\text{NH}_4^+$ -rich reverse osmosis (RO) brine, enhancing the  $\text{NH}_3$  recovery rate by 17 times and halving electrical energy consumption. An electrodialysis (ED) cell is added in Fig. 6e for concentrating  $\text{NO}_3^-$  and  $\text{NH}_4^+$  to provide a greater driving force for reaction and separation, which effectively enhances the rates of  $\text{NO}_3^-$  removal and  $\text{NH}_3$  recovery by 10 and 95 times, respectively. Moreover, Co(DIM) is added in the concentrated  $\text{NO}_3^-$  solution instead of wastewater in this ED-concentrated parallel configuration for preventing catalysts from separating from the wastewater.

### 3.3 Catalyst design for large-scale wastewater treatment

For industrial treatment of  $\text{NO}_x^-$ -containing wastewater, it is necessary to take into account the concentrated electrolyte, the pH of electrolytes and the electrode amplification for improving the economic viability of electrosynthesis.<sup>107–110</sup> Currently, the  $\text{NO}_x^-$  concentration is typically lower than 1 M in a majority of efforts. Fig. 7a shows the nonmonotonic change of  $\text{NH}_3$  yield on  $\text{Cu}_2\text{O}$  from 0.01 to 3 M  $\text{NO}_3^-$ . In the dilute regime (0.01 to 0.1 M), the production rate increases with nitrate concentrations due to promoted mass transfer and reaction kinetics. However, a decline is experienced in the range from 0.1 to 3 M, which is caused by the excessive  $\text{NO}_3^-$  adsorption for reducing water molecule adsorption on surface sites. To solve the dilemma of mismatched reaction kinetics between the HER and  $\text{NO}_3^-$



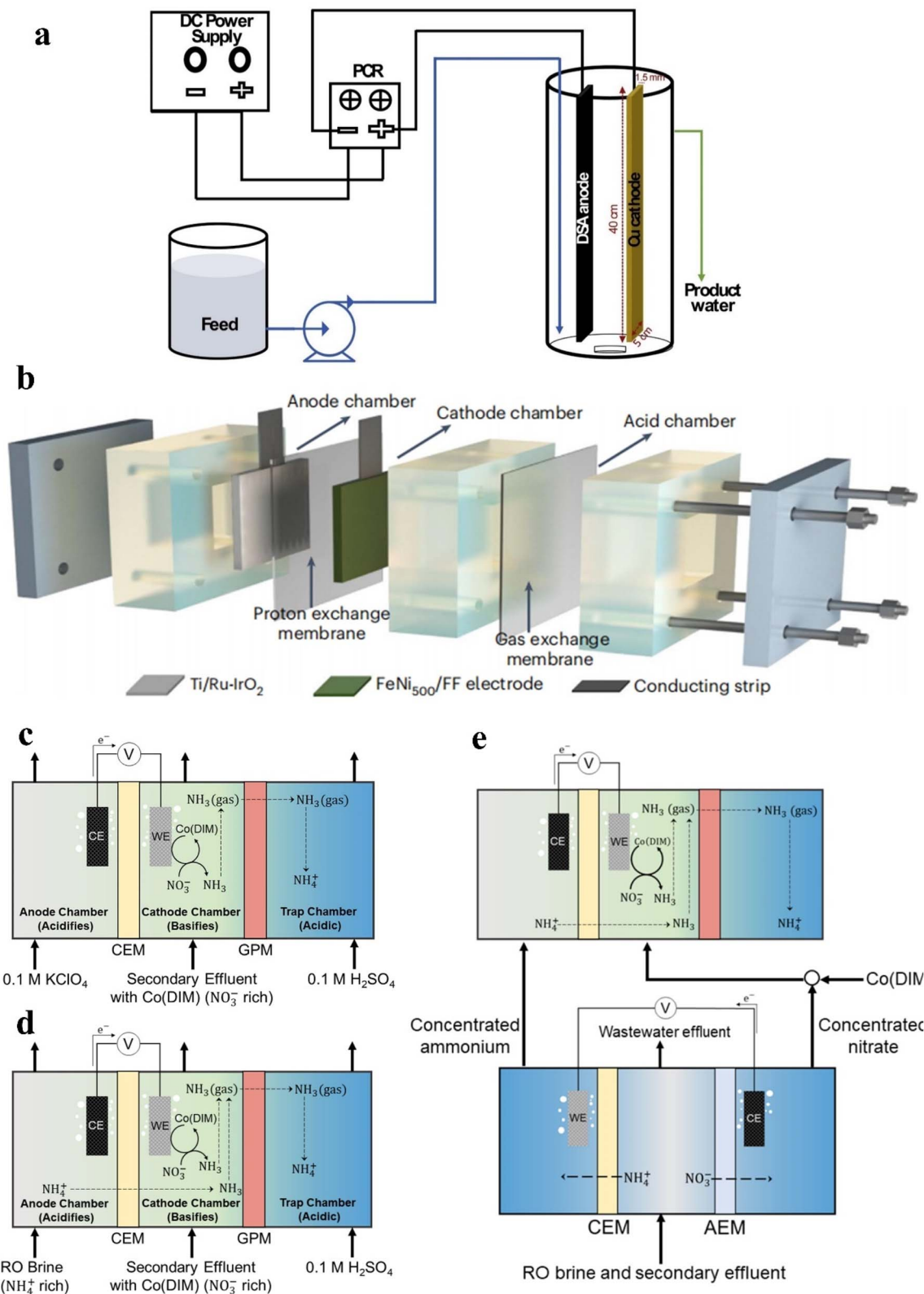


Fig. 6 (a) Electrochemical continuous flow system. Reproduced with permission.<sup>106</sup> Copyright 2020, Elsevier. (b) Schematic of the three-chamber membrane distillation reactor. Reproduced with permission.<sup>5</sup> Copyright 2023, Springer Nature. (c) The ECS reactor, (d) ECS reactor with  $\text{NH}_4^+$ -rich RO brine and (e) ECS reactor with ED. Reproduced with permission.<sup>107</sup> Copyright 2023, American Chemical Society.



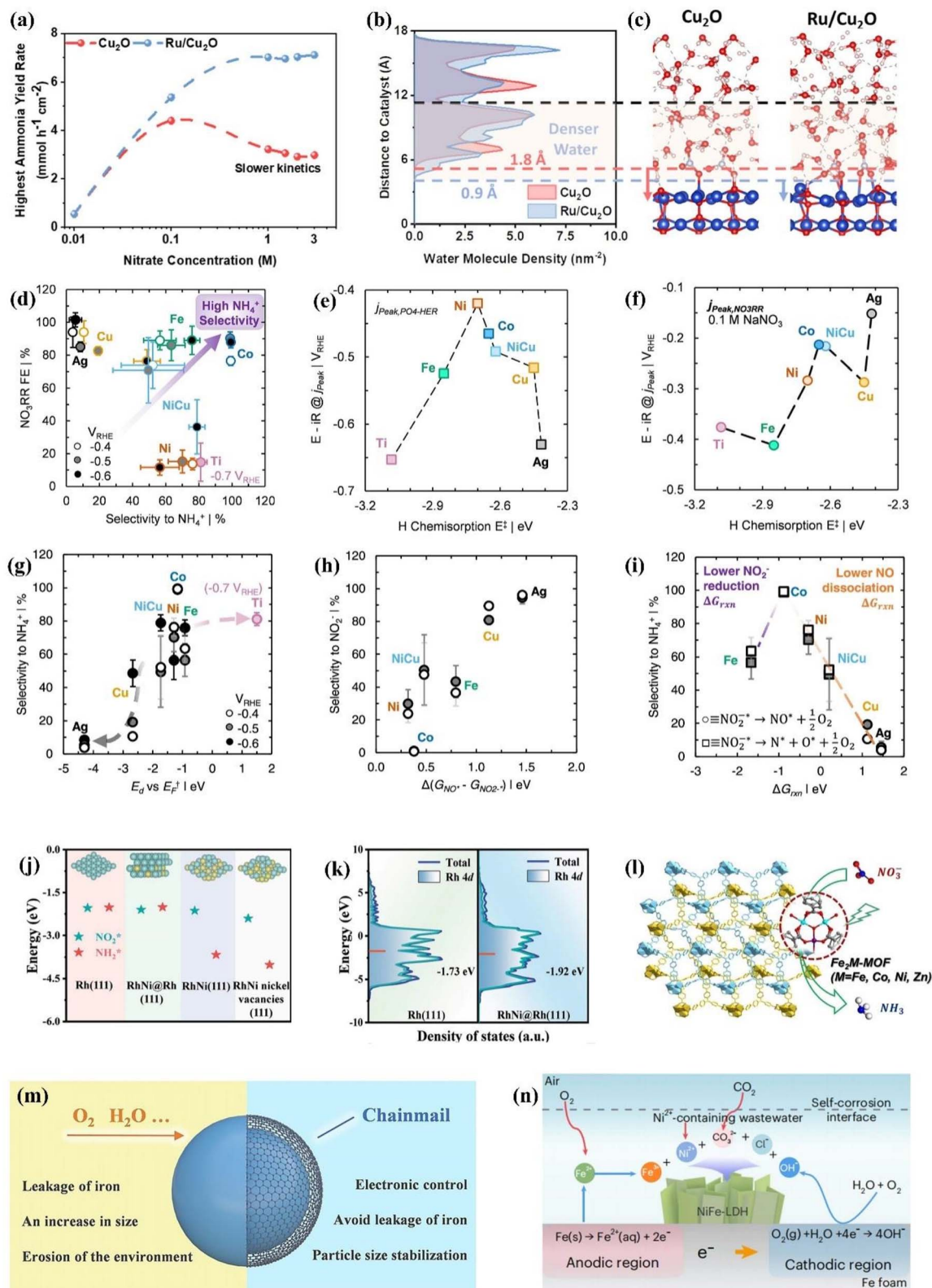


Fig. 7 (a) Optimized  $\text{NH}_3$  yield rate of various catalysts in an electrolyte containing 1 M KOH and different  $\text{NO}_3^-$  concentrations and (b) densities of water molecules, and (c) representative molecular dynamics simulation snapshots. Reproduced with permission.<sup>111</sup> Copyright 2024, American Chemical Society. (d)  $\text{NO}_3^-$  reduction FE and selectivity on different metals. Relationships between the H chemisorption energy and potential in mass-transfer limited (e) phosphate-mediated HER and (f)  $\text{NO}_3^-$  reduction in 0.1 M  $\text{NaNO}_3$ . (g) Relationship between selectivity and  $E_d$  vs.  $E_f$ . Relationship between reaction free energies ( $\Delta G_{\text{rxn}}$ ) for converting  $\text{NO}_2^*$  to  $\text{NO}$  and selectivity to (h)  $\text{NO}_2^-$  and (i)  $\text{NH}_4^+$ . Reproduced with permission.<sup>112</sup> Copyright 2022, American Chemical Society. (j) Adsorption energy of  $\text{NO}_2^*$  and  $\text{NH}_2^*$  and (k) d-band centers of different catalysts. Reproduced with permission.<sup>113</sup> Copyright 2024, Wiley-VCH. (l) 3D framework of  $\text{Fe}_2\text{M-MOF}$ . Reproduced with permission.<sup>114</sup> Copyright 2023, Wiley-VCH. (m) The role of graphene nano-chainmail. Reproduced with permission.<sup>115</sup> Copyright 2023, Wiley-VCH. (n) The specific reactions of the self-corrosion process. Reproduced with permission.<sup>5</sup> Copyright 2023, Springer Nature.



reduction, Ru is introduced in Cu<sub>2</sub>O for more efficient NO<sub>3</sub><sup>-</sup> reduction.<sup>111</sup> The water density profiles from the Cu<sub>2</sub>O and Ru/Cu<sub>2</sub>O surface are exhibited in Fig. 7b and c through molecular dynamics simulations. The higher H<sub>2</sub>O density in the Ru/Cu<sub>2</sub>O model is more conducive to promoting the collision between NO<sub>3</sub><sup>-</sup> ions and H<sub>2</sub>O molecules for more efficient hydrogen transfer, which endows Ru/Cu<sub>2</sub>O with 89% NH<sub>3</sub> FE under 9.9 A for 3 M NO<sub>3</sub><sup>-</sup> reduction.

As for the amplified synthesis of electrodes, the electrode pieces are often present individually on a laboratory scale, so if they were to be scaled up directly, not only would there be modification, but also the internal resistance would increase. The direct amplification of electrodes faces the challenges of technical limitation for processing and sharp increases in resistance; the stacked electrode module mentioned in Fig. 5h provides a decent solution for avoiding the limitations induced by direct electrode amplification. Despite the extremely wide range of pH values in sewage collected, the majority of sewage is in neutral and acid environments. The catalysts discussed in Section 2 are designed for alkaline conditions; the HER competition will be more intense in neutral and acidic media than that in alkaline media.

As for the catalysts in a neutral environment, a series of transition metals and alloys have been explored including Ti, Fe, Co, Ni, Cu, Ag and Ni<sub>0.68</sub>Cu<sub>0.32</sub>, employing 0.1 M Na<sub>x</sub>H<sub>3-x</sub>PO<sub>4</sub> solution to simulate the neutral environment.<sup>112</sup> The promising catalysts have been screened under neutral conditions with exploration of the associated thermodynamic and kinetic parameters of catalysts. As demonstrated in Fig. 7d, metallic Co exhibits promising NO<sub>3</sub><sup>-</sup> reduction FE and selectivity for NH<sub>3</sub> formation. Co with moderate H chemisorption energy (Fig. 7e and f) shows smaller cathode mass transfer limiting the nitrate reduction potential compared with transition metals binding H strongly such as Fe and Ti, indicating that strong H chemisorption energy leads to sluggish proton-coupled electron transfer and hydrogenation kinetics in NO<sub>3</sub><sup>-</sup> reduction. Further explorations of the origin of the excellent Co activity are demonstrated in Fig. 7g-i by probing the d-band center energy ( $E_d$ ) and calculated reaction free energies of NO<sub>2</sub><sup>-</sup> reduction to NO and further dissociation. The theoretical calculations have confirmed that more negative  $\Delta G_{\text{NO}_{\text{ads}}}$  can be achieved when  $E_d$  approaches the Fermi level ( $E_F$ ), which is caused by the increasingly unoccupied antibonding molecular orbital formed between NO<sub>ads</sub> and the catalyst surface. However, as illustrated in Fig. 7g, Co exhibits superior selectivity beyond 95% over a broad range of potentials, which significantly exceeds the selectivity of metals (Ni, Fe) with similar  $E_d$  vs.  $E_F$ . The calculated reaction free energies of NO<sub>2</sub><sup>-</sup> reduction to NO and further dissociation (Fig. 7h and i) are considered for better exploring the origin of the extraordinary NH<sub>3</sub> selectivity of Co. As described in Fig. 7h, the selectivity for NO<sub>2</sub><sup>-</sup> decreases roughly with the reduced difference between  $\Delta G_{\text{NO}}$  and  $\Delta G_{\text{NO}_2^-}$ . In spite of the lower NO<sub>2</sub><sup>-</sup> reduction energy barrier in Ni compared to Co, Ni exhibits inferior NH<sub>3</sub> selectivity due to weaker decomposition for subsequently produced NO. In contrast, the lower NH<sub>3</sub> selectivity of Fe possessing more favourable NO dissociation is caused by adverse NO<sub>2</sub><sup>-</sup> reduction

activity. The volcanic trend of selectivity is described in Fig. 7i based on NO<sub>2</sub><sup>-</sup> reduction activity and NO dissociation energy of metals explored. An ideal state of catalysts with promising NH<sub>3</sub> selectivity can be represented by Co with sufficiently strong tendency for NO binding and dissociation and adequate activity for NO<sub>2</sub><sup>-</sup> reduction.

The design of excellent catalysts can be conducted by approaching a series of parameters on Co including hydrogen affinity and  $E_d$  vs.  $E_F$ . For example, in spite of high hydrogen binding energy of the NiFe alloy for unfavorable NO<sub>3</sub><sup>-</sup> reduction, the NiFe alloy possesses  $E_d$  vs.  $E_F$  and work function similar to Co, which cause better NO<sub>3</sub><sup>-</sup> reduction activity and selectivity than the mono-component metals (Ni, Fe). On the flip side, the performance of Co can also be further improved including the possible improvement of the energy conversion efficiency. Enhancing NO<sub>3</sub><sup>-</sup> affinity by pairing of metal oxides and electrolyte modulation are both effective approaches for boosting the NO<sub>3</sub><sup>-</sup> reduction activity of Co.

As for the catalysts under acidic conditions, there are major challenges including (1) stronger HER competition and (2) drastically reduced stability caused by the dissolution of metal catalysts in strong acidic environments.<sup>110,111</sup> However, several advantages are also presented in acidic environments, which can avoid the subsequent extraction process and spillage loss of aqueous NH<sub>3</sub> owing to the direct generation of nitrogen fertilizers such as (NH<sub>4</sub>)<sub>2</sub>SO<sub>4</sub> and NH<sub>4</sub>Cl under acidic conditions.<sup>112</sup> In order to resist acid-induced corrosion, Rh has recently been employed to construct an electrocatalyst and is one of the few metals that can withstand aqua regia. The RhNi@Rh bimetallics are synthesized for weakening the adsorption of NO<sub>2</sub><sup>\*</sup> and NH<sub>2</sub><sup>\*</sup> to resist adsorption-induced Rh dissolution (Fig. 7j), which exhibit a declined d-band center (Fig. 7k) due to the compressive stress induced from the inside out by the RhNi alloy core. With the modified adsorption behavior of Rh, the catalyst demonstrates exceptional stability over an extended 400 h test in acidic environments.

The immobilisation also provides a plausible strategy for enhancing the stability of transition metal catalysts capable of effectively inhibiting the HER. Fe<sub>2</sub>Co-MOF (Fig. 7l) is obtained by assembling Fe<sub>2</sub>Co clusters and H<sub>4</sub>TPBD ligands,<sup>115</sup> which bypasses the decreased catalytic efficiencies due to saturated metal centres in the majority of MOFs. Fe<sub>2</sub>Co-MOF exhibits superior electrocatalytic stability up to 75 h at -1.1 V vs. RHE in pH = 1 electrolyte, accompanied by NH<sub>3</sub> yield approaching 20 653.5 μg h<sup>-1</sup> mg<sub>site</sub><sup>-1</sup> and FE of 90.55%. The decent activity of Fe<sub>2</sub>Co-MOF derives from the suppressed HER and high turnover adsorption of NO<sub>3</sub><sup>-</sup> due to the unsaturated metal sites induced by trinuclear clusters. In addition, the catalytic efficiency is further enhanced in acidic environments filled with protons, since the transfer of electrons and reactants can be promoted by the redox-active dinitrogen ligand. The remarkable stability of Fe<sub>2</sub>Co-MOF can be primarily ascribed to the highly connected structure with robust coordinative bonds formed by the combination of high-valence Fe<sup>3+</sup> and carboxylate ligands.

In addition to the approach mentioned above, armoured catalysts and self-corrosion reconstruction strategies also deserve to be utilized for enhancing long-term stabilities in the



acid environment. Fig. 7m depicts the merits of armoured catalysts for  $\text{NO}_3^-$  conversion to  $\text{N}_2$  protected by ultrathin graphene nanolayers, which could provide more insights for enhancing the stabilities of  $\text{NO}_x^-$  reduction catalysts.<sup>115</sup> Moreover, novel insights on expanding electrocatalyst and wastewater treatment can be provided by the economical self-corrosion approach (Fig. 7n) utilizing heavy metal ions in wastewater ( $\text{Ni}^{2+}$ ,  $\text{Co}^{2+}$  and  $\text{Zn}^{2+}$ ) for inducing the Fe surface to generate LDH nanosheets.<sup>5</sup> This corrosion strategy is conducive to generating the active phase and avoiding conventional corrosion passivation. Furthermore, the contact between active sites and  $\text{NO}_x^-$  is facilitated in the corroded interface with an enlarged and turbulent region.

## 4. Production of multiple value-added chemicals

The comfortable survival of human beings in contemporary society is ensured by the mass production of organic N-containing compounds. Currently, more than half of the  $\text{NH}_3$  produced globally is consumed in organic N-containing compounds produced industrially by thermo-catalyzed reactions under harsh conditions (150–500 °C, 20–250 bar), causing disruptions in global carbon and nitrogen cycles due to the excess emissions of  $\text{CO}_2$  and nitrogen oxides ( $\text{NO}_x$ ).<sup>116</sup> Recently, with the creation of the carbon-neutral vision and the boom of  $\text{CO}_2$  reduction and  $\text{NO}_x^-$  reduction, electrocatalytic C–N coupling reactions based on  $\text{NO}_x^-$  reduction have proposed new horizons for achieving the synthesis of high-value organic N-containing compounds, which employ useless or harmful wastes including C-containing species ( $\text{CO}_2$ , CO) and N-containing species ( $\text{NO}_2^-$ ,  $\text{NO}_3^-$ ).<sup>117</sup> A brighter future is emerging for electrocatalytic synthesis than traditional thermo-catalytic synthesis due to the sustainability and more favourable on-site/on-demand production owing to the features of decentralisation and modularity.<sup>118</sup>

More intriguingly, the hidden surprises of  $\text{NO}_x^-$  reduction extend far beyond the synthesis of high-value organic N-containing compounds. The H-type electrolyser commonly employed in the laboratory offers an uninterrupted environment for  $\text{NO}_x^-$  reduction and also provides an opportunity for the anodic reaction to be thoroughly explored.<sup>119</sup> The anodic oxygen evolution reaction (OER) commonly coupled with the  $\text{NO}_x^-$  reduction reaction has motivated researchers to seek alternative anodic reactions including small organic molecule oxidation reaction with low energy consumption and appealing products,<sup>120,121</sup> which is caused by high energy barriers and difficult collection of products in the OER. Therefore, current research advances and potential challenges will be discussed in this section on the C–N coupling reactions and alternative anodic reactions based on  $\text{NO}_x^-$  reduction.

### 4.1 C–N coupling reactions

The C–N coupling reactions based on  $\text{NO}_x^-$  reduction can be categorized into coupling and cascade reactions, and the difference between tandem reaction and integrated reaction is

illustrated in Fig. 8a. The integrated reaction is achieved by coupling key intermediates to build preset chemical bonds and generate advanced products, while tandem electrocatalytic reactions employ the *in situ* desorbed products.<sup>122</sup> The integrated reaction based on  $\text{CO}_2$  and  $\text{NO}_3^-$  reduction is commonly used for the synthesis of urea. Indeed, the  $\text{NO}_2^-$  reduction process has also been confirmed to be promoted by  $\text{CO}_2$  on copper catalysts,<sup>123</sup> which can reach a drastically enhanced  $\text{NH}_3$  FE of approximately 100% within a wide range of potentials. The significantly enhanced  $\text{NO}_2^-$  reduction performance is due to  $\text{CO}_{\text{ads}}$  generated by  $\text{CO}_2$  reduction, which accelerates the deoxygenation and subsequent hydrogenation of intermediates.

The C–N coupling reaction demonstrates promising prospects for the synthesis of high value N-containing chemicals; however, a number of challenges are faced such as sluggish kinetics and low selectivity due to stubborn bonding structures of the reactants and competition of  $\text{CO}_2/\text{NO}_2^-/\text{NO}_3^-$  reduction and the HER.<sup>75</sup> Numerous factors can exert an influence on electrocatalytic C–N coupling, including reactants, electrocatalysts and the reactors. The reactors have already been discussed in Fig. 5. The research status and the existing challenges of the C–N coupling reaction will be discussed in the part including the related reaction mechanisms and design principles of catalysts, hopefully providing a comprehensive understanding of C–N coupling reactions based on  $\text{NO}_x^-$  reduction.

#### 4.1.1 Formation of compounds with C(=O)–N bonds.

Amides are a group of compounds with a characteristic C(=O)–N unit, which can be constituted by CO and  $\text{NH}_y$  intermediates. Amides available currently based on  $\text{CO}/\text{CO}_2$  reduction and  $\text{NO}_x^-$  reduction include urea, formamide, and acetamide. The possible reaction pathways of forming C(=O)–N bonds are demonstrated in Fig. 8b employing various C-containing species.

**4.1.1.1 Urea.** Urea accounts for approximately 70% of nitrogen-containing manure in the world, contributing to the sustainable development of human society.<sup>124</sup> However, it is primarily obtained through the combination of  $\text{NH}_3$  and  $\text{CO}_2$  under harsh conditions, which is adverse to alleviating fossil energy consumption and decreasing  $\text{CO}_2$  emissions.<sup>125</sup> The synthesis of urea from  $\text{CO}_2$  and  $\text{NO}_3^-/\text{NO}_2^-$  has recently been considered as a mild alternative route, but the current production efficiency is struggling to reach the standard for industrial applications.<sup>126</sup> Thus, emphasis will be placed here on the formation mechanism of urea and the related studies on catalysts, in order to promote the industrial application process of electrocatalytic urea synthesis.

An in-depth understanding of the reaction mechanism of electrocatalytic urea synthesis is beneficial for improving the efficiency of the reaction. Numerous studies have been reported on the reaction mechanisms of electrocatalytic urea synthesis (Fig. 9), with controversies mainly existing in the key intermediates of C–N coupling. In this section, three representative mechanisms are introduced. It was proposed the formation of  $^*(\text{NH}_2)\text{CO}$  intermediates from  $^*\text{CO}$  and  $^*\text{NH}_2$  as a key step in C–N coupling through comparative experiments for the co-reduction of  $\text{CO}_2 + \text{NH}_3$  and  $\text{CO} + \text{NO}_2^-$ .<sup>126</sup> Meng *et al.* proposed that urea was generated by the coupling of  $^*\text{NH}_2$  and



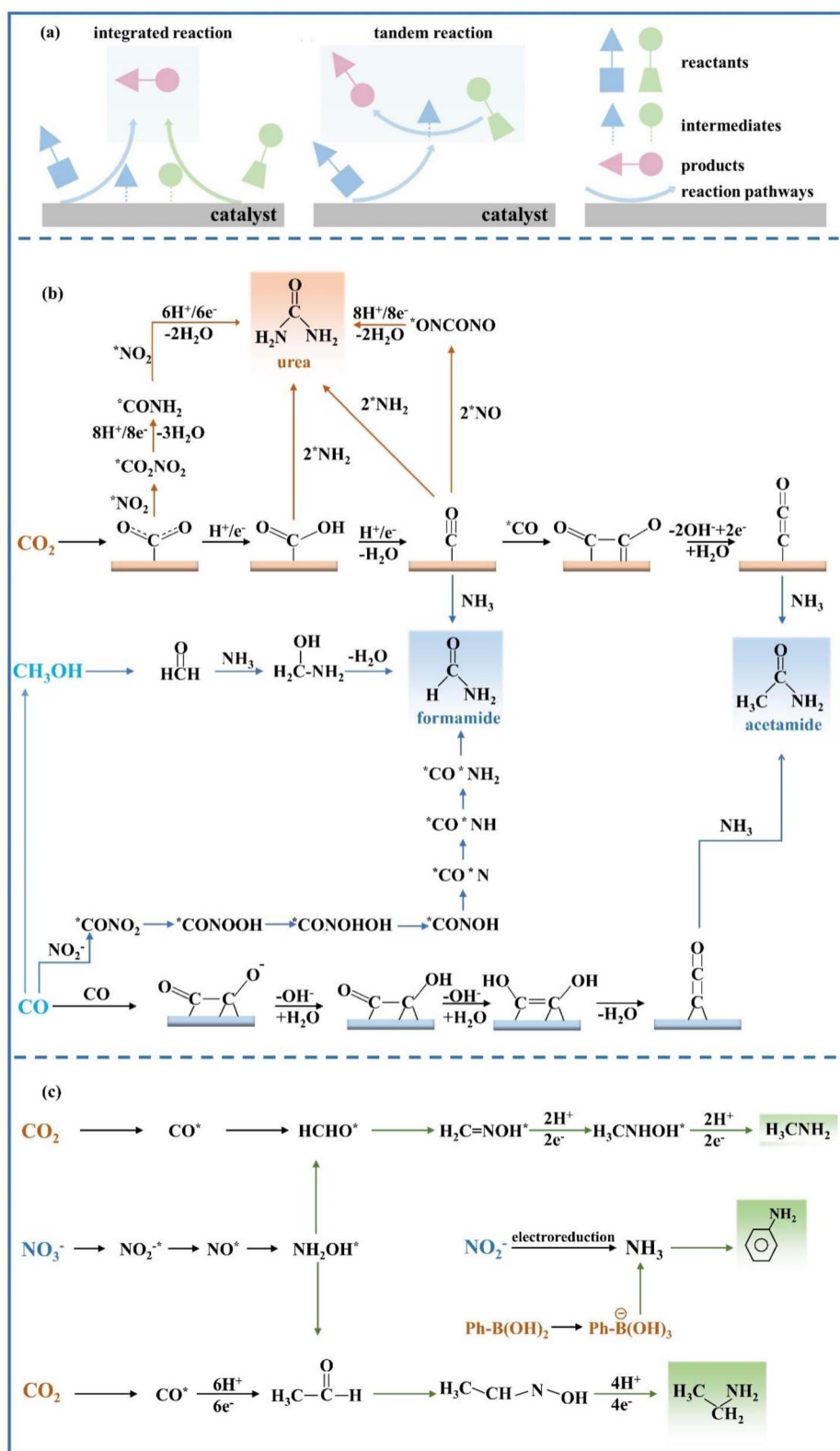


Fig. 8 (a) Schematic diagrams of tandem reaction and integrated reaction. Reaction pathways of (b) C(=O)-N bond formation and (c) C-N bond formation.

\*COOH intermediates in  $\text{NO}_2^-$ -integrated  $\text{CO}_2$  reduction,<sup>127</sup> which was inferred from the disappearance of the signal peaks of \*COOH in *in situ* diffuse reflectance infrared Fourier

transform spectroscopy during the coexistence of  $\text{CO}_2$  and  $\text{NO}_2^-$ . Meanwhile, Yu *et al.* proposed that the intermediates in  $\text{NO}_3^-$ -integrated  $\text{CO}_2$  reduction are \* $\text{NO}_2^-$  and \* $\text{CO}_2$  instead of



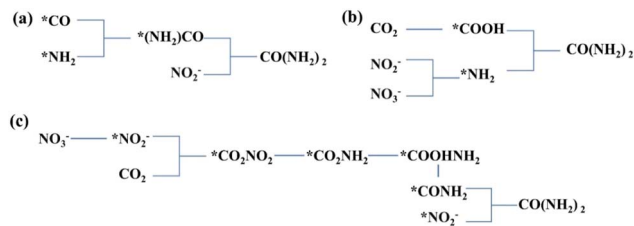


Fig. 9 (a–c) Possible mechanisms of CO-reducing electrocatalytic synthesis of urea by  $CO_2$  and  $NO_2^-/NO_3^-$ .

$*CO$  and  $*NH_2$ .<sup>128</sup> The early coupling of  $*NO_2^-$  and  $*CO_2$  forms  $*CO_2NO_2$ , and subsequently, the  $*CO_2NO_2$  intermediate undergoes several electron and proton transfer steps to generate  $*CO_2NH_2$ . The later protonation of the  $*CO_2NH_2$  intermediate to  $*COOHNH_2$  is considered as the potential determining step (PDS) in the urea electrocatalytic synthesis process.

Despite the various controversies surrounding the current mechanisms, it is definitely evident that the adsorption configuration of  $CO_2$  can have a significant impact on the activity and selectivity of the urea synthesis reaction. The adsorption configurations of intermediates for the reaction can be modulated by the charged state of the catalyst surface with changes in catalyst compositions. Cu–In catalysts possessing different charge states were developed to explore the influences of different  $CO_2$  adsorption configurations on the activity and selectivity of the electrocatalytic synthesis of urea.<sup>129</sup> The urea yield on a negatively charged  $Cu_{97}In_3-C$  catalyst with a C-bound surface was approximately thirteen times that of the positively charged  $Cu_{30}In_{70}-C$  catalyst possessing an O-bound surface. It was confirmed that the subsequent C–N coupling process was facilitated by the C-bound configuration ( $*COOH$ ) on the catalyst surface, while the O-bound configuration ( $*OCHO$ ) was a terminal blocking further non-electrochemical steps and causing inferior performance of urea formation.

With the further studies on the mechanisms of urea electrocatalytic synthesis, the focus on urea electrocatalytic synthesis has shifted to the pursuit of high FE catalysts.<sup>130–132</sup> In contrast, the focus on other C–N coupling reaction organics has remained on exploring more synthetic pathways and expanding the variety of obtained N-containing organics, while less emphasis has been placed on the development of catalysts and Cu-based catalysts available commercially have usually been chosen directly. A diverse variety of catalysts have currently been developed for urea production including bimetallic catalysts, metal oxide catalysts, and monoatomic catalysts. Obviously, decent electrocatalysts with enhanced conductivity and abundant active sites are favourable to promote the simultaneous reduction of  $CO_2$  and  $NO_3^-/NO_2^-$ . Bimetallic electrocatalysts have exhibited promising performance in urea electrocatalytic synthesis, which is caused by the fact that the binding energy of the reaction intermediates can be controlled by modifying the electronic structure and composition of electrocatalysts.<sup>133–135</sup> For example, Te-doped Pd nanocrystals significantly promoted the reaction between  $*CO$  and  $*NH_2$  in the reaction process of  $CO_2$  and  $NO_2^-$  and inhibited the formation of  $N_2$  through  $NO_2^-$

reduction owing to the synergistic effect between Te and Pd.<sup>136</sup> The synergistic effect of bimetallic electrocatalysts was also demonstrated for specific morphological and structural regulation. Self-supported core–shell Cu@Zn nanowires, obtained by a simple electroreduction process, reached a higher urea yield rate of  $7.29 \mu mol cm^{-2} h^{-1}$  and a corresponding faradaic efficiency of 9.28% compared to Zn ( $0.77 \mu mol cm^{-2} h^{-1}$ , 1.00%) and Cu ( $0 \mu mol cm^{-2} h^{-1}$ , 0.00%).<sup>135</sup> Theoretical calculations revealed that the catalytic performance of urea electrocatalytic synthesis was enhanced by electron transfer from the Zn shell to the Cu core due to the reduction in the critical coupling energy barriers of the  $*CO$  and  $*NH_2$  intermediates. In comparison to metal catalysts, metal oxide catalysts were prone to introduce oxygen vacancies that acted as catalytic centres with rich electron densities.<sup>137</sup> Oxygen vacancy-rich anatase  $TiO_2$  (Cu– $TiO_2$ ) nanotubes could be easily obtained by low-valence Cu doping,<sup>138</sup> and the high-density oxygen vacancies facilitated the selectivity of  $NO_x$  to  $*NH_2$  and exposure of bi- $Ti^{3+}$  active sites.

For single-atom catalysts anchoring isolated atoms on carriers by ligands, they have aroused growing interest due to the optimal atom utilization, the explicit catalytic active sites and the absence of aggregated metal atoms.<sup>139</sup> Leverett *et al.* prepared Cu–N–C single-atom catalysts for electrocatalytic urea synthesis and studied the effect of Cu coordination on the electrocatalytic reduction reactions of  $CO_2$  ( $CO_2RR$ ) and  $NO_3^-$  ( $NO_3RR$ ).<sup>140</sup> The experiments combined with theoretical calculations indicate that the Cu– $N_4$  site exhibited higher activity for the  $CO_2RR$ , while the Cu– $N_{4-x}-C_x$  site demonstrated a higher  $NH_4^+$  yield rate in the  $NO_3RR$ . The catalyst on the Cu– $N_4$  site exhibited the best urea synthesis performance with an FE of 28% and a yield of  $4.3 nmol s^{-1} cm^{-2}$  at  $-0.9 V$  versus RHE. In contrast to isolated single-atom catalysts, bonded diatomic catalysts thermodynamically and kinetically strengthen pivotal C–N coupling due to the presence of effective sites for coordinated adsorption and coactivation of carbon and nitrogen sources. The bonded diatomic Fe–Ni catalyst demonstrated excellent performance, reaching a high urea yield of  $20.2 mmol h^{-1} g^{-1}$  with FE of 17.8%,<sup>141</sup> which was up to an order of magnitude higher than those of single-atom and isolated diatomic electrocatalysts. Such excellent performance is mainly due to two factors: (1) the simultaneous introduction of Fe and Ni sites overcomes the restriction of unilateral selective adsorption and activation of carbon or nitrogen reactants. (2) The bridge sites of Fe–Ni pairs boost the C–N coupling process thermodynamically and kinetically, and the bridged configuration inhibits the HER effectively.

The metal-based catalysts mentioned above have exhibited promising performance; nonetheless, metal-based catalysts are still hampered by high cost,<sup>142</sup> destabilization under adverse operating conditions<sup>143</sup> and vulnerability to small molecule toxicity.<sup>144</sup> Carbon-based metal-free electrocatalysts have shown brilliant application prospects in the electrocatalytic synthesis of urea due to abundant sources, competitive cost and superior stability. The doping of heteroatoms such as N, B and F has been widely employed for optimizing the electrocatalytic properties of carbon materials for urea synthesis due to new surface charge distribution induced by doping. The HER activity can be



suppressed in carbon materials doped with F, facilitating enhanced urea synthesis activity. The high urea yield rate of carbon nanotubes with a fluorine-rich surface (F-CNT) could reach up to  $6.36 \text{ mmol g}_{\text{cat}}^{-1} \text{ h}^{-1}$ , which has been confirmed to be caused by more favorable  $^*\text{COOH}$  generation and  $^*\text{NH}_2$  formation processes on the F-CNT.<sup>143</sup> The abundant nitrogen-containing active intermediates are also more conducive for urea synthesis. The remarkable urea yield rate of  $610.6 \text{ mg h}^{-1} \text{ g}_{\text{cat}}^{-1}$  was exhibited in porous N-doped carbon obtained by pyrolysis of the coordination polymer, which even exceeded those of some noble metal-based catalysts.<sup>145</sup>

The synthesis of urea by simultaneous electrochemical reduction of  $\text{CO}_2$  and  $\text{NO}_2^-/\text{NO}_3^-$  has gained growing attention, especially when the coupled  $\text{CO}_2\text{RR}$  is of high significance for achieving carbon neutrality. However, the synthesis mechanisms are full of arguments. In regard to studies on catalysts, numerous experiments in the design of high-performance catalysts have confirmed that it is imperative to attach importance to the coactivation and reaction of reactants, as well as the construction of efficient sites conducive to C–N coupling by optimizing the adsorption of intermediate components. Nevertheless, the Faraday efficiencies of current catalysts for urea synthesis are generally lower than 70%,<sup>146</sup> which are far from the actual requirements. Furthermore, the precise regulation of the interfacial microenvironment should not be ignored for comprehensively improving the electrocatalytic performance, since efficient and stable three-phase interfaces are required to supply reactants and accelerate mass transfer.<sup>147</sup> Three optimization strategies can be employed for controlling the microenvironment, including adjusting the hydrophobicity of electrocatalysts, improving proton supply in the electrolyte and regulating experimental conditions in the electrolyzer.

**4.1.1.2 Organic amides.** Amides including formamide and acetamide are of significant commercial value, and are widely employed in polymer manufacture and biological compounds. In view of the energy crisis and environmental pollution aggravated by the current industrial synthesis of amides, electrocatalytic routes have been developed employing  $\text{CO}_2$  and  $\text{NH}_3$ . The combination of  $\text{NH}_3$  in the liquid phase and  $\text{CO}_2$  in the gas phase has been proven to successfully synthesize formamides and acetamides over non-homogeneous Cu catalysts,<sup>148</sup> the detailed mechanisms are shown in Fig. 8b. However, the FEs obtained are considerably low, not even exceeding 1% at the highest. In addition, the electrolysis process will be disrupted by the undesired carbonate formation at the electrode-electrolyte interface, owing to the inevitable reaction of  $\text{OH}^-$  ions with  $\text{CO}_2$  under alkaline conditions.

In order to solve such dilemma, CO reduction is a promising strategy to replace direct  $\text{CO}_2$  reduction, which can yield CO from electrochemical  $\text{CO}_2$  reduction under non-alkaline conditions. The higher selectivity for acetic acid in CO reduction has been demonstrated compared to  $\text{CO}_2$  reduction on the Cu catalyst surface, implying an easy reaction between the ketene intermediates in the CO reduction process with the nucleophilic agent  $\text{NH}_3$ . The FE of generating acetamide can reach 40% at  $-0.68 \text{ V vs. RHE}$  on the Cu nanoparticle catalyst, when the molar ratio of CO to  $\text{NH}_3$  is up to 2 : 1.<sup>149</sup> The synthesis

mechanism and competitive reactions for acetamide formation are shown in Fig. 8b. Under the conditions of high pH and less negative potential, CO reduction is more biased towards the generation of the  $\text{C}=\text{C}=\text{O}$  intermediate compared with the generation of the  $\text{C}=\text{COH}$  intermediate for producing ethylene and ethanol. Although the formation of ethylene and ethanol is inhibited at high  $\text{NH}_3$  concentration, the formation of acetamide is also faced with competition for forming acetate due to  $\text{OH}^-$  on the surface of the catalyst.

The N-containing nucleophilic reagent in the above C–N coupling pathways directly employs  $\text{NH}_3$ . With the flourishing of studies on  $\text{NO}_2^-$  reduction to  $\text{NH}_3$  due to the low dissociation energy of the  $\text{N}=\text{O}$  bond ( $204 \text{ kJ mol}^{-1}$ ), a credible route is provided for green  $\text{NH}_3$  production with renewable electricity. Electrocatalytic coupling of  $\text{NO}_2^-$  with CO has been confirmed to be an alternative avenue to achieve formamide synthesis. The reaction pathway is shown in Fig. 8b for electrocatalytic coupling of  $\text{NO}_2^-$  with CO obtained by theoretical calculation, and the key challenge for reaching decent formamide selectivity is the construction of highly active and stable catalysts for enhancing CO and  $\text{NO}_2^-$  activity reduction and promoting C–N coupling. Ru atoms dispersed on Cu nanoclusters (Ru–Cu) have been developed to achieve decent formamide FE of 45.65% with a yield of  $2483.77 \text{ } \mu\text{g h}^{-1} \text{ mg}_{\text{cat}}^{-1}$  at  $-0.5 \text{ V vs. RHE}$ .<sup>150</sup> The design of dual active sites in Ru–Cu catalysts could achieve synergistic catalysis for C and N activation, which can significantly improve the C–N coupling efficiency compared to monometallic catalysts. The adsorption and subsequent hydrogenation process of  $\text{NO}_2^-$  could be promoted by Ru atoms, while the dissociation adsorption of CO could be accelerated by adjacent Cu sites. Therefore, the decent activity and selectivity for formamide formation can be reached by the synergistic catalysis in Ru–Cu catalysts.

The electrocatalytic C–N coupling system developed currently is generally employed under aqueous conditions, and the further enhancement of C–N coupling efficiency is limited by severe HER competition due to the low-soluble CO in the aqueous solution. The extremely water-soluble methanol can be obtained from CO conversion, which can be an attractive alternative C-containing species for C–N coupling reactions. The combination of methanol and  $\text{NH}_3$  has provided an interesting process to produce formamide under ambient conditions, which utilizes the nucleophilic attack of  $\text{NH}_3$  on a formaldehyde-like intermediate from methanol electro-oxidation. The most likely reaction pathway is illustrated in Fig. 8c. The C–N bond formation in formamide is caused by a nucleophilic attack process, where the positively charged C in  $^*\text{CH}_2\text{O}$  is attacked by the electronegative N atom in  $\text{NH}_3$ . The conversion of methanol and  $\text{NH}_3$  to formamide can reach a selectivity of 74.26% and FE of 40.39% on  $\text{PtO}_2$  at  $100 \text{ mA cm}^{-2}$ .<sup>151</sup> The decent formamide production efficiency was due to the moderate affinity of the reaction intermediate on  $\text{PtO}_2$ . However, the large-scale production of formamides based on methanol and  $\text{NH}_3$  is faced with the limitation of poor mass transfer at high current density exceeding  $100 \text{ mA cm}^{-2}$ . Compared with the easy dissolution of precious metal Pt under large oxidation current density, a boron-doped diamond (BDD)



electrode is highly promising for large-scale formamide electro-synthesis due to the outstanding stability on the most corrosive electrolytes with a wide potential window.<sup>152</sup> The BDD electrode exhibits high durability after a continuous 20-cycle test on a laboratory scale, which also shows decent FE of 33.5% and output of 36.9 g h<sup>-1</sup> at 264 A in the pilot plant test.

The combination of methanol and ammonia has provided a favorable idea for the electrochemical synthesis of formamide, and this strategy has been proven to be extensible for the synthesis of other organic N compounds. More intriguingly, acetamide and propenamide can be obtained by lengthening

the C chain of C-containing species, and formyl methylamine can be obtained by replacing the N source (CH<sub>3</sub>NH<sub>2</sub>).

#### 4.1.2 Formation of compounds with C-N bonds.

Numerous co-reduction experiments with CO<sub>2</sub> and NO<sub>2</sub><sup>-</sup>/NO<sub>3</sub><sup>-</sup> have successfully generated urea, which demonstrates the potential of producing organonitrogen compounds. Nevertheless, the current scope of reaction products requires further broadening to produce more high-value chemicals, such as alkylamines. Wang *et al.* has made breakthroughs in the co-reduction of CO<sub>2</sub> and NO<sub>3</sub><sup>-</sup> to produce alkylamines, including

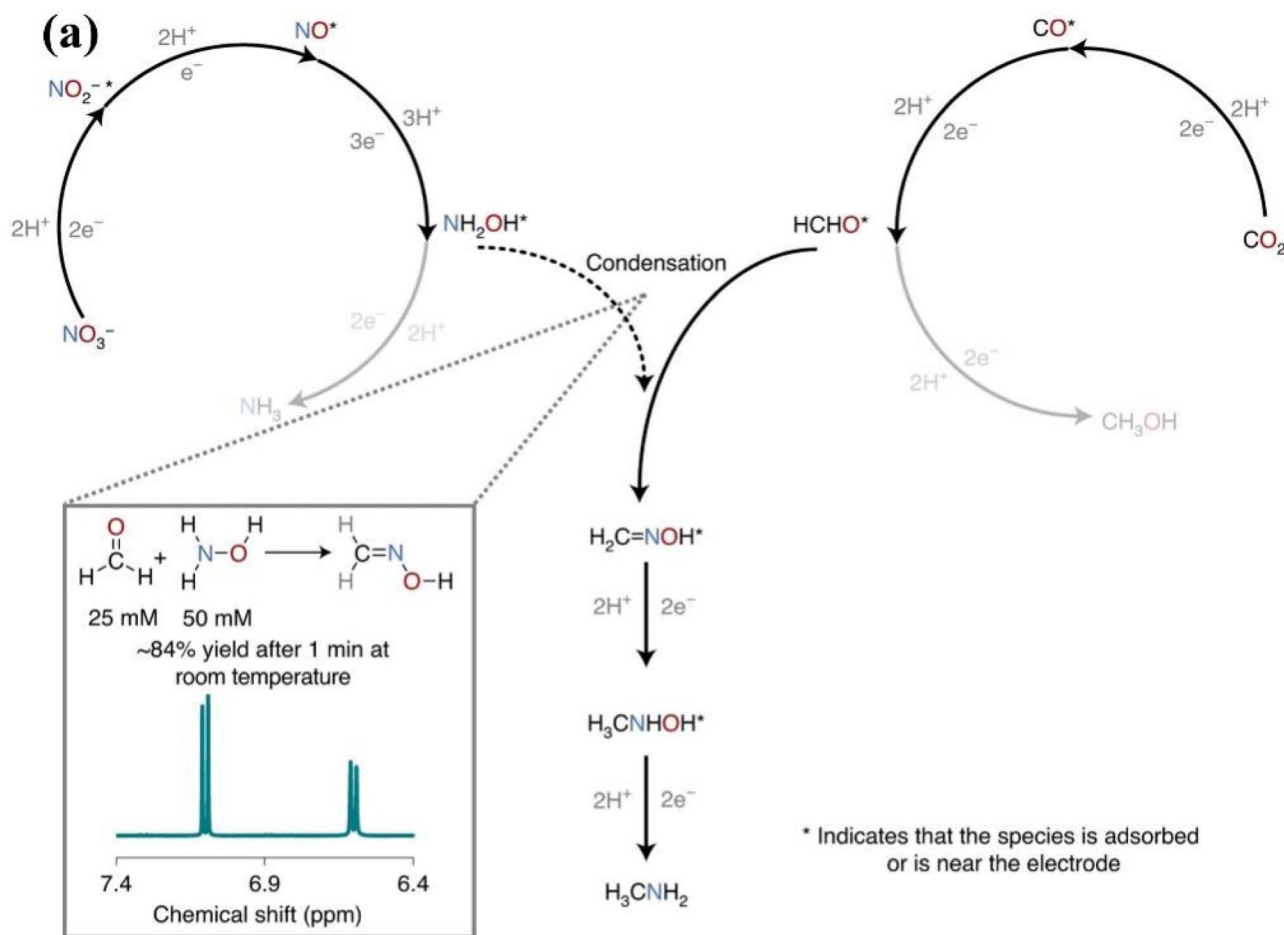


Fig. 10 (a) The proposed reaction pathways to form methylamine. Reproduced with permission.<sup>29</sup> Copyright 2021, Springer Nature. (b) Reaction pathways for obtaining ethylamine. Reproduced with permission.<sup>155</sup> Copyright 2022, Elsevier.



methylamine<sup>29</sup> and ethylamine,<sup>153</sup> involving more advanced catalysts with novel C–N coupling mechanisms.

Methylamine is the simplest alkylamine and is employed as the major commercial chemical intermediate in pesticide production, solvent fabrication and water treatment.<sup>154</sup> For industrial production, methylamine is currently obtained from methanol (CH<sub>3</sub>OH) and NH<sub>3</sub> under high-temperature high-pressure conditions. CoPc-NH<sub>2</sub>/CNT was developed as a working electrode for driving the co-reduction process of CO<sub>2</sub> and NO<sub>3</sub><sup>−</sup> to methylamine involving the transfer of 14 electrons and 15 protons.<sup>29</sup> The total FE of the co-reduction process reaches 13%, with no performance degradation after at least 16 hours of uninterrupted operation. More significantly, the intermediates (NH<sub>2</sub>OH and HCHO) involved in the key C–N coupling step are confirmed; thus, eight consecutive reaction steps regarding the formation of methylamine are proposed. As shown in Fig. 10a, formaldoxime is generated by spontaneous condensation through NH<sub>2</sub>OH derived from NO<sub>3</sub><sup>−</sup> with HCHO obtained from CO<sub>2</sub>, and then formaldoxime is reduced to form methylamine.

The synthesis of ethylamine is obviously more challenging than that of methylamine, which is caused by the process of transferring 20 electrons and 21 protons in total. The cascade electrocatalytic synthesis of ethylamine from CO<sub>2</sub> and NO<sub>3</sub><sup>−</sup> is achieved by the catalysis of oxide-derived Cu nanoparticles.<sup>153</sup> In addition, the related synthesis mechanism is proposed. The mechanism of ethylamine synthesis displayed in Fig. 10b is similar to that of methylamine, and the critical C–N coupling step is the condensation of hydroxylamine (NH<sub>2</sub>OH) with aldehyde (CH<sub>3</sub>CHO) to form acetaldoxime. However, the FE of ethylamine production by this process is as low as 0.3%. The poor yield of ethylamine is primarily attributed to the following factors: (1) it is adversely affected by the competition between the rapid side reactions of NH<sub>2</sub>OH to NH<sub>4</sub><sup>+</sup> and CH<sub>3</sub>CHO to CH<sub>3</sub>CH<sub>2</sub>OH. (2) The reduction rate of acetaldoxime is significantly slower than that of the CO<sub>2</sub>RR, NH<sub>3</sub>RR and HER. (3) The selectivity of the CO<sub>2</sub> to CH<sub>3</sub>CHO reduction pathway on Cu-based catalysts is inferior.

While significant breakthroughs have been made in the synthesis of methylamine and ethylamine, it is hard to implement them immediately in industry. Apparently, the electrocatalytic synthesis of propylamines or alkylamines with more C atoms will also be more arduous. The route for generating arylamine has recently been explored by coupling arylboronic acid with NH<sub>3</sub> produced from NO<sub>2</sub><sup>−</sup> reduction. Intriguingly, the synthesis of arylamine was carried out at pulsed potentials,<sup>156</sup> which was owing to the consideration that metal electrodes were easily reduced to zero-valent metals during NO<sub>2</sub><sup>−</sup> reduction and deactivated due to excessive oxidation in the C–N coupling process. Therefore, low-coordinated Cu nano-coral was employed under pulse potential for efficient NO<sub>2</sub><sup>−</sup> reduction and C–N coupling, which experienced an alternating transition from the zero-valent state to the divalent state.

**4.1.3 Other possible products.** Expanding the possible range of C–N bonds that can be formed has been a hot topic to obtain more abundant and high value-added organic nitrogen compounds.<sup>150</sup> It is evident from the synthetic routes discussed

Table 2 Possible organonitrogen products with corresponding C sources and N sources

C source	N source	Organonitrogen compound
CO	NH <sub>3</sub>	Acetamide
CO	CH <sub>3</sub> NH <sub>2</sub>	<i>N</i> -Methylacetamide
CO	C <sub>2</sub> H <sub>5</sub> NH <sub>2</sub>	<i>N</i> -Ethylacetamide
CO	(CH <sub>3</sub> ) <sub>2</sub> NH	<i>N,N</i> -Dimethylacetamide

above that the majority of the synthetic pathways proposed have been essentially based on nucleophilic attack of N-containing species on C-containing species, which hints at the opportunity of obtaining more abundant N-containing organics by altering the N and C sources. For example, it has been proven to be possible to form alanine by replacing the C source with pyruvic acid,<sup>157</sup> which is coupled with NH<sub>2</sub>OH intermediates during NO<sub>3</sub><sup>−</sup> reduction.

The environmental pollutant CO could be a promising C source substituting CO<sub>2</sub>, which facilitates environmental restoration and averts the disruption of the electrolysis process due to undesirable carbonate formation from the inevitable reaction of OH<sup>−</sup> with CO<sub>2</sub> at the electrode–electrolyte interface. The possible C and N sources and the corresponding theoretical products are depicted in Table 2, presumably contributing to the broadening of the organonitrogen product scope to obtain more high-value products.

#### 4.2 Valuable anode reactions coupled with NO<sub>x</sub><sup>−</sup> reduction

The traditional NO<sub>x</sub><sup>−</sup> reduction reaction is usually coupled with the OER, which consumes up to 90% of the input energy and produces low-value O<sub>2</sub>.<sup>158</sup> The OER with high energy consumption results in twice the production cost of the electrocatalytic NH<sub>3</sub> production compared to the conventional Haber–Bosch route for producing NH<sub>3</sub> with the same quality.<sup>2</sup> Currently, appeals to develop alternative oxidation reactions are progressively increasing for enhancing energy utilization efficiency and obtaining value-added chemicals. The development of anodic oxidation reactions employing inexpensive or hazardous reactants has received considerable attention. Electrooxidation of N<sub>2</sub> to HNO<sub>3</sub> is a promising alternative reaction, which can both generate high-value HNO<sub>3</sub> and provide reactants for NO<sub>x</sub><sup>−</sup> reduction.<sup>119</sup> In spite of the inferior FE of only 1.23% for N<sub>2</sub> oxidation on Pt foil,<sup>159</sup> this strategy employing anodic N<sub>2</sub> oxidation has provided a promising route for obtaining HNO<sub>3</sub> and NH<sub>3</sub> at distributed sources.

In addition, the immense interest in electrooxidation reactions of biomass and related derivatives has been driven not only by lower theoretical potentials than those of the OER (Fig. 11) but also by the sustainable nature for accelerating the creation of a carbon-neutral society.<sup>160</sup> Biomass and its derivatives have been considered as renewable carbon-neutral resources including 5-hydroxymethylfurfural, glycerol and benzyl alcohol with abundant proton content.<sup>161–165</sup> Commercial Ni foam was usually employed as an anode in earlier studies for initially verifying the feasibility of replacing the anodic reaction. With the deeper cognition on electrocatalytic reconfiguration,



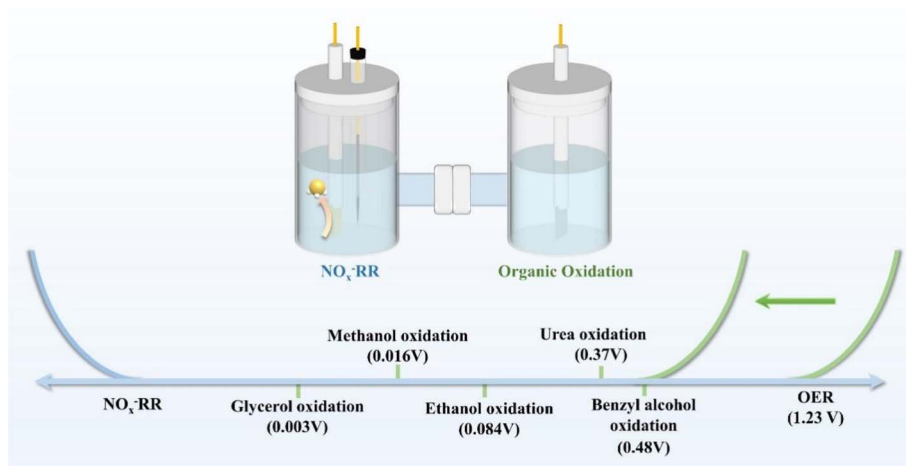


Fig. 11 Thermodynamic equilibrium potentials of several oxidation reactions.

excellent bifunctional catalysts can be obtained by adjusting the reconfiguration direction of catalysts in different reaction processes.<sup>166</sup> Decent bifunctional NiCu based catalysts have been developed for  $\text{NO}_3^-$  reduction and glycerol oxidation reactions, which can be reconstructed under different operating conditions.<sup>167</sup> Under the cathodic reduction environment, the materials were transformed into amorphous  $\text{Ni}(\text{OH})_2$  coupled Cu nanoparticles. The  $\text{NO}_3^-$  reduction performance of the material was enhanced by the synergistic effect of Cu and  $\text{Ni}(\text{OH})_2$ . Meanwhile, composites including NiOOH and CuO with rich Cu vacancies were obtained by the reconstruction of NiCu based catalysts during the glycerol oxidation process. The glycerol oxidation process was promoted by the increased exposure of active NiOOH species due to the leaching of Cu in Cu vacancy-rich CuO. Compared to the traditional electrolyzer coupled with the OER, the electrolyzer coupled with the GOR exhibited an incredible overpotential reduction of 285 mV at a current density of  $100 \text{ mA cm}^{-2}$ .

Recently, some efforts have been focussed on further improving the economic efficiency of electrochemical systems coupled with  $\text{NO}_3^-$  reduction and glycerol oxidation. A  $\text{CO}_2$  capture strategy has been explored for upgrading products,<sup>168</sup> which can convert anodic formate to potassium diformate and cathodic  $\text{NH}_3$  to  $\text{NH}_4\text{HCO}_3$ . This strategy is conducive to product separation holding promising prospects for industrial applications.

The strategy of replacing the OER with biomass electro-oxidation has provided an innovative insight for reducing electricity consumption and enhancing product value. However, biomass electrooxidation also faces the challenges of higher cost and higher requirements for membrane, which typically drives current density below  $200 \text{ mA cm}^{-2}$  under potential exceeding 1.23 V.<sup>169–171</sup> The undesirable overpotential in the biomass electrooxidation process may be attributed to the high energy required for destroying C–H and O–H bonds in biomass.<sup>172,173</sup> Compared to the C–H and O–H bonds in alcohols or aldehydes, more easily dissociated hydrogen atoms are manifested in the more reactive enol structure.<sup>174</sup> Consequently, substances including ascorbic acid with a highly active enol

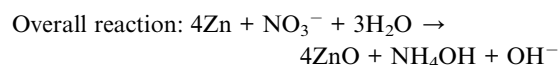
structure can be considered as an anode additive to accelerate  $\text{NH}_3$  production in future efforts.

## 5. Energy conversion and storage systems

Metal- $\text{NO}_2^-/\text{NO}_3^-$  batteries have received growing attention as a paradigm of simultaneous  $\text{NH}_3$  production and energy output.<sup>175–178</sup> The anodes currently employed in metal- $\text{NO}_2^-/\text{NO}_3^-$  batteries are dominated by Zn anodes, which are especially appealing in the treatment of industrial wastes containing  $\text{NO}_2^-/\text{NO}_3^-$  due to their low cost, easy recycling and high stability in alkaline solutions.<sup>179</sup> The working mechanism, performance, hurdles and opportunities of Zn- $\text{NO}_2^-/\text{NO}_3^-$  batteries are primarily discussed in this section.

### 5.1 Metal- $\text{NO}_3^-$ batteries

In 2021, the viability of galvanic metal- $\text{NO}_3^-$  batteries (Fig. 12a) was evidenced by Zhi's group for the first time, shedding renewed light on the field of sustainable  $\text{NH}_3$  generation and zinc-based batteries.<sup>21</sup> A Pd-doped  $\text{TiO}_2$  nanoarray was employed as the cathode in this experiment, which exhibited impressive  $\text{NO}_3^-$  reduction activity due to attenuated intermediate adsorption (Fig. 12b) with introducing Pd. The electrochemical reactions of the discharge process in this Zn- $\text{NO}_3^-$  cell are as follows:



However, the rechargeability of Zn- $\text{NO}_3^-$  batteries has not been sufficiently investigated in the Zn- $\text{NO}_3^-$  battery with Pd-doped  $\text{TiO}_2$  as the cathode. Lin *et al.* have developed rechargeable Zn- $\text{NO}_3^-$  batteries (Fig. 12c), inspired by soybean which could exploit nitrogen and generate oxygen simultaneously.



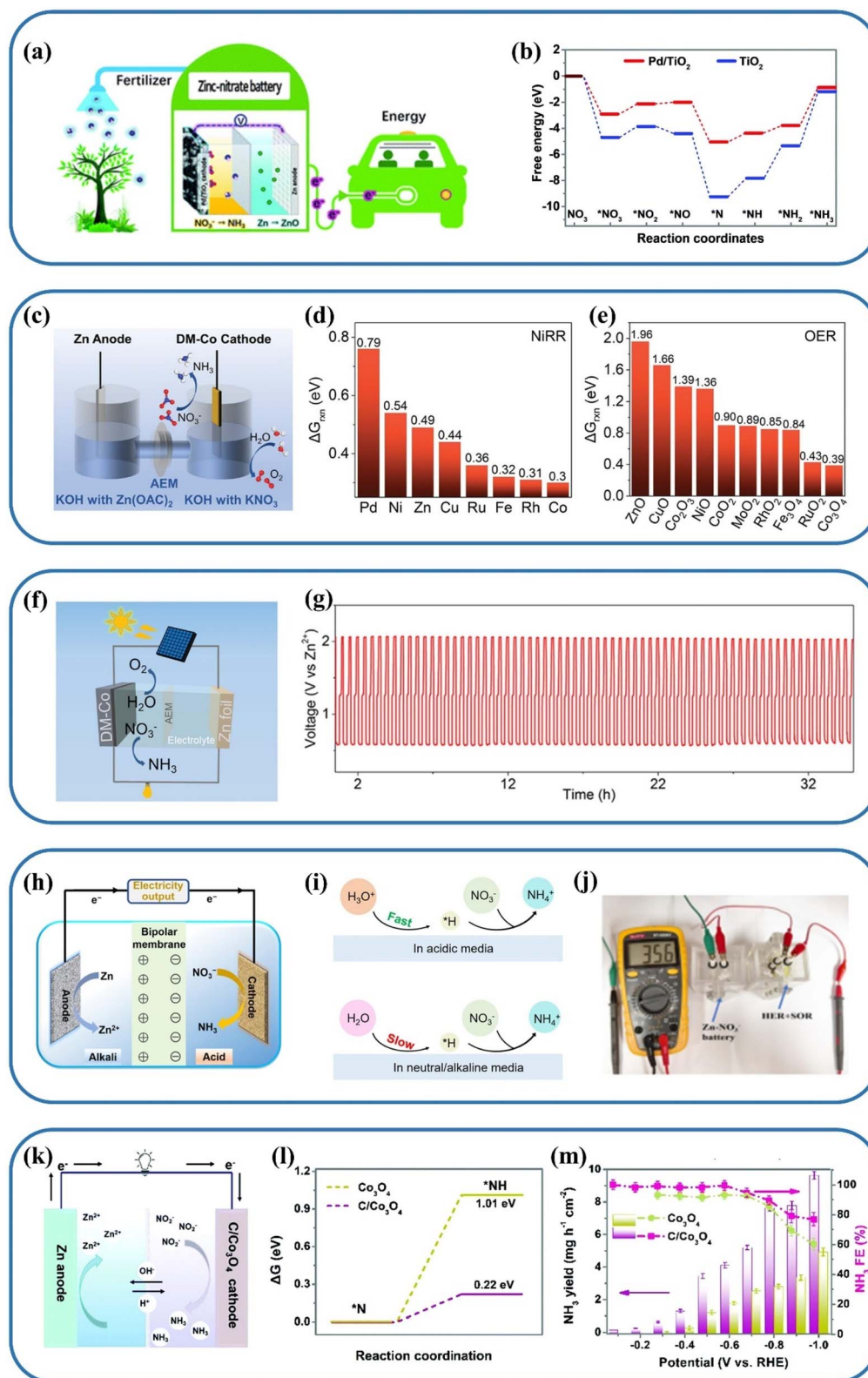
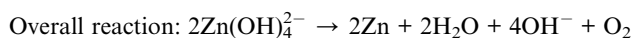
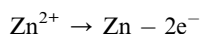


Fig. 12 (a) Schematic representation of the Zn–NO<sub>3</sub><sup>−</sup> battery, (b) the calculated intermediate adsorption energies on Pd/TiO<sub>2</sub>. Reproduced with permission.<sup>21</sup> Copyright 2021, Royal Society of Chemistry. (c) Schematic diagram of a rechargeable Zn–NO<sub>3</sub><sup>−</sup> battery. Catalyst screening studies of (d) the NO<sub>3</sub>RR and (e) OER. (f) Photovoltaic driven Zn–NO<sub>3</sub><sup>−</sup> battery. (g) Galvanostatic discharge–charge cycling curves of a Zn–NO<sub>3</sub><sup>−</sup> battery assembled from DM-Co. Reproduced with permission.<sup>180</sup> Copyright 2022, Wiley-VCH. (h) Schematic diagram of an alkaline–acidic hybrid Zn–NO<sub>3</sub><sup>−</sup> battery. (i) Pathways for active hydrogen production in the NO<sub>3</sub><sup>−</sup>RR process under different conditions. (j) Environmental sulfur recovery powered by a hybrid Zn–NO<sub>3</sub><sup>−</sup> battery. Reproduced with permission.<sup>181</sup> Copyright 2023, Springer Nature. (k) Schematic diagram of a Zn–NO<sub>2</sub><sup>−</sup> battery. (l) The energy barriers of C/Co<sub>3</sub>O<sub>4</sub> and Co<sub>3</sub>O<sub>4</sub> for the rate-determining step in the NO<sub>2</sub>RR. (m) NO<sub>2</sub>RR performance of C/Co<sub>3</sub>O<sub>4</sub> at different potentials. Reproduced with permission.<sup>23</sup> Copyright 2022, Royal Society of Chemistry.



Bifunctional DM-Co catalysts were designed for the NO<sub>3</sub>RR and OER after theoretical pre-screening (Fig. 12d and e), which reveals the great potential of Co-based catalysts.<sup>180</sup> The aqueous rechargeable Zn–NO<sub>3</sub><sup>−</sup> battery constructed with DM-Co as the cathode achieves a high power density of over 25 mW cm<sup>−2</sup>, which is much higher than that of the Zn–NO<sub>3</sub><sup>−</sup> battery with a Pd-doped TiO<sub>2</sub> cathode (0.87 mW cm<sup>−2</sup>). In addition, the successive discharge–charge cycle curves illustrated in Fig. 12g reveal the excellent robustness of the rechargeable Zn–NO<sub>3</sub><sup>−</sup> battery, presenting 76 cycles at a low potential of 2.1 V. The discharge process in this rechargeable Zn–NO<sub>3</sub><sup>−</sup> cell is analogous to that of the Zn–NO<sub>3</sub><sup>−</sup> cell with a Pd-doped TiO<sub>2</sub> cathode.

The following reactions take place when the aqueous Zn–NO<sub>3</sub><sup>−</sup> battery is charged:



The total battery reaction of the rechargeable Zn–NO<sub>3</sub><sup>−</sup> cell can be described as follows:



It is worth mentioning that the Zn–NO<sub>3</sub><sup>−</sup> battery system driven by a photovoltaic cell (Fig. 12f) has also been attempted. When the Zn–NO<sub>3</sub><sup>−</sup> battery is charged, the electrical energy is stored in the chemical bonds of the Zn anode, which is converted from the solar energy absorbed by the photovoltaic cell. The optimal NO<sub>3</sub>RR FE of 95% and solar-to-NH<sub>3</sub> efficiency of 19.5% are obtained in the Zn–NO<sub>3</sub><sup>−</sup> cell system driven by a photovoltaic cell. The cells described above are operated in alkaline environments; however, corrosion issues of equipment and limitations on the type of battery components are unavoidable under extreme pH conditions.<sup>182</sup> A Zn–NO<sub>3</sub><sup>−</sup> cell with a Co<sub>2</sub>AlO<sub>4</sub> cathode has also recently been constructed in a neutral environment,<sup>40</sup> which is also beneficial for simulating the actual textile wastewater environment. The introduction of Al ions improves Co<sub>2</sub>O<sub>4</sub> with poor ammonia production performance in a neutral environment, which achieved optimal adsorption of NO<sub>3</sub><sup>−</sup> on Co sites by reducing the electron cloud density on the Co surface. The power density of 3.43 mW cm<sup>−2</sup> offered by the Zn–NO<sub>3</sub><sup>−</sup> battery was higher than that of the Zn–NO<sub>3</sub><sup>−</sup> battery reported for the first time. However, the output voltages are limited in current Zn–NO<sub>3</sub><sup>−</sup> batteries equipped with NO<sub>3</sub><sup>−</sup> reduction under neutral/alkaline conditions, which indicates more challenges on the conditions of the cathodic part severely affecting the power density and NH<sub>3</sub> yield of the related battery. Recently, an alkaline–acidic hybrid Zn–NO<sub>3</sub><sup>−</sup> battery (Fig. 12h) is developed to exhibit higher output power density, due to enhanced NO<sub>3</sub><sup>−</sup> conversion rate and more energy-efficient NH<sub>3</sub> generation with abundant protons provided in

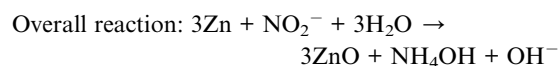
an acidic environment (Fig. 12i). FePc/TiO<sub>2</sub> is developed as a stable and active electrocatalyst for energy-efficient acid NO<sub>3</sub><sup>−</sup> reduction with an impressive NH<sub>3</sub> yield rate of 17.4 mg h<sup>−1</sup> cm<sup>−2</sup> and NH<sub>3</sub> FE of 90.6%.<sup>181</sup> The developed alkaline–acid hybrid Zn–NO<sub>3</sub><sup>−</sup> battery based on the FePc/TiO<sub>2</sub> cathode shows high open-circuit voltage up to 1.99 V with high power density of 91.4 mW cm<sup>−2</sup>, which can be applied for efficient environmental sulfur recovery by driving the electrolyzer composed of cathodic HER and anodic sulfur oxidation reaction with the current density of 35.6 mA cm<sup>−2</sup> (Fig. 12j).

Some progress has been made in terms of rechargeability studies of Zn–NO<sub>3</sub><sup>−</sup> batteries and the design of cathodes under different conditions. However, the performance of the cells requires further enhancement and the electrolyte environment in the cells should be brought closer to that of real wastewater. Notably, the potential value of the NO<sub>3</sub>RR under basic conditions is 0.6 V vs. the RHE, which is higher than the 0.4 V of the oxygen reduction reaction (ORR) O<sub>2</sub> + 2H<sub>2</sub>O + 4e<sup>−</sup> → 4OH<sup>−</sup>.<sup>183</sup> Consequently, NO<sub>3</sub><sup>−</sup>-based batteries potentially produce a higher voltage output than metal–air batteries. The performances of Zn–NO<sub>3</sub><sup>−</sup> batteries and Zn–air batteries as reported in current literature are presented in Table 3. It is clear that a significant discrepancy can be found between the performance of the Zn–NO<sub>3</sub><sup>−</sup> batteries and the Zn–air batteries; reducing the discrepancy can be achieved by seeking decent efficiency and high-selectivity catalysts and developing more Zn–NO<sub>3</sub><sup>−</sup> batteries with an abundant electrolyte environment.

## 5.2 Metal–NO<sub>2</sub><sup>−</sup> batteries

The cathode conditions of Zn–NO<sub>2</sub><sup>−</sup> batteries (Fig. 12k) developed currently are an alkaline environment and neutral environment,<sup>177</sup> and the cathode reaction in the alkaline environment is identical to that in the neutral environment. Carbon-doped Co<sub>3</sub>O<sub>4</sub> nanotubes have been developed as cathodic catalysts under neutral conditions for the assembly of novel Zn–NO<sub>2</sub><sup>−</sup> batteries.<sup>23</sup> During the NO<sub>2</sub><sup>−</sup> reduction process, the energy barrier of \*N hydrogenation in C/Co<sub>3</sub>O<sub>4</sub> (Fig. 12l) is significantly reduced due to accelerated charge transfer caused by the C dopant inducing a local electric field. Carbon-doped Co<sub>3</sub>O<sub>4</sub> possessed decent catalytic activity (Fig. 12m) for NO<sub>2</sub><sup>−</sup> reduction, achieving a high FE approaching 100% for ammonia production within a wide range (−0.1 V to −0.6 V vs. RHE). The assembled Zn–NO<sub>2</sub><sup>−</sup> battery demonstrated a power density of 6.03 mW cm<sup>−2</sup> and a FE of 95.1% for NH<sub>3</sub> production.

The electrochemical reactions in the Zn–NO<sub>2</sub><sup>−</sup> battery are presented as follows:



Some advances have been made in Zn–NO<sub>2</sub><sup>−</sup> batteries with cathodes under neutral and alkaline conditions. Indeed, little



Table 3 Comparison of the performance between Zn-NO<sub>2</sub><sup>-</sup>/NO<sub>3</sub><sup>-</sup> batteries and various Zn-based batteries

Batteries	Catalyst	OCV (V)	FE (%)	NH <sub>3</sub> yield (mg h <sup>-1</sup> cm <sup>-2</sup> )	Power density (mW cm <sup>-2</sup> )	Ref.
Zn-NO <sub>3</sub> <sup>-</sup>	Pd/TiO <sub>2</sub>	0.81	81.3	0.54	0.87	21
Zn-NO <sub>3</sub> <sup>-</sup>	ZnCo <sub>2</sub> O <sub>4</sub>	0.6	98.33	1.55	4.62	22
Zn-NO <sub>3</sub> <sup>-</sup>	Fe/Ni <sub>2</sub> P	1.22	85	4.17	3.25	176
Zn-NO <sub>3</sub> <sup>-</sup>	Co <sub>2</sub> AlO <sub>4</sub>	1.862	92.6	0.75	3.43	40
Zn-NO <sub>3</sub> <sup>-</sup>	NiCo <sub>2</sub> O <sub>4</sub> /CC	1.30	96.1	0.82	3.94	175
Zn-NO <sub>3</sub> <sup>-</sup>	CeO <sub>2-x</sub> @NC	1.45	96.09	2.46	3.44	184
Zn-NO <sub>3</sub> <sup>-</sup>	DM-Co	0.62	91	2.04	25	180
Zn-NO <sub>3</sub> <sup>-</sup>	CuNi NPs/CF	0.94	97.03	94.57	70.7	185
Zn-NO <sub>3</sub> <sup>-</sup>	FePc/TiO <sub>2</sub>	1.99	88.2	12.3	FePc/TiO <sub>2</sub>	181
Zn-NO <sub>2</sub> <sup>-</sup>	TiO <sub>2-x</sub>	0.6	91.1	12.230	2.38	177
Zn-NO <sub>2</sub> <sup>-</sup>	C/Co <sub>3</sub> O <sub>4</sub>	1.589	95.1	0.802	6.03	23
Hydrazine-nitrate	Bimetallic RuCo	—	—	6.64	12	178
Zn-N <sub>2</sub>	CoPi/NPCS	~1.4	16.35	0.0147	0.49	186
Zn-N <sub>2</sub>	OV-Ti <sub>2</sub> O <sub>3</sub>	—	19.29	0.03724	1.02	187
Zn-N <sub>2</sub>	VN@NSC-900	~0.55	—	0.000172	0.01642	18
Zn-N <sub>2</sub>	CoPi/HSNPC	~1	24.42	—	0.31	188
Zn-N <sub>2</sub>	NbS <sub>2</sub>	0.5	10.12	0.03758	0.31	189
Zn-N <sub>2</sub>	Fe <sub>1.6</sub> HTNs	—	—	0.00014	0.028	190
Zn-NO	MoS <sub>2</sub>	2.03	85.0	0.4118	1.04	191
Zn-NO	CoS <sub>1-x</sub>	1.83	53.62	1.49	2.06	192
Zn-NO	Bi@C	2.08	93	0.36	2.35	193
Zn-O <sub>2</sub>	S-FeCo <sub>3</sub> P/NPSG	—	—	—	38	194
Zn-O <sub>2</sub>	Fe@Co-NMC	—	—	—	98.7	195
Zn-O <sub>2</sub>	AP-CONPs/NF	1.37	—	—	89.1	196

effort has been devoted to catalysts in acidic environments, while the theoretical voltage (2.146 V) of the Zn-NO<sub>2</sub><sup>-</sup> cell in the acidic environment is higher than those in alkaline (1.089 V) and neutral environments (1.589 V). Furthermore, a bottleneck currently exists in the development of rechargeable Zn-NO<sub>2</sub><sup>-</sup> batteries, which may be due to the challenge in avoiding the OER coinciding with the conversion of nitrite to nitrate.

### 5.3 Hurdles and opportunities on batteries

The comparative performances of the currently developed Zn-NO<sub>2</sub><sup>-</sup> batteries, Zn-NO<sub>3</sub><sup>-</sup> batteries and Zn-gas batteries are exhibited in Table 3, thus providing a better understanding of the development status of Zn-NO<sub>2</sub><sup>-</sup> batteries and Zn-NO<sub>3</sub><sup>-</sup> batteries. It is evident that Zn-NO<sub>x</sub><sup>-</sup> batteries are much more promising than Zn-N<sub>2</sub> for simultaneous NH<sub>3</sub> generation and electricity output. However, the insufficiently desirable state of current Zn-NO<sub>x</sub><sup>-</sup> batteries must also be confirmed. Strategies to improve the performance of Zn-NO<sub>x</sub><sup>-</sup> batteries cannot be limited in designing more advanced cathode catalysts with reduced HER competition.<sup>197</sup> As shown in Table 3, despite facing fierce competition from the HER, the FEs for Zn-NO<sub>x</sub><sup>-</sup> batteries range from 81.3% to 98.3%, which suggests that the HER at most leads to 1.7–18.7% loss in FE. In view of the higher theoretical voltage of the Zn-NO<sub>x</sub><sup>-</sup> cell and more abundant proton supply in an acidic environment, it is essential to develop a Zn-NO<sub>x</sub><sup>-</sup> cell with acidic cathodic NO<sub>x</sub><sup>-</sup> reduction and enhance the corrosion resistance of the corresponding electrodes for effectively increasing the open circuit voltage and power density.

Moreover, pure metallic Zn electrodes are widely employed in rechargeable battery systems, including zinc-air, silver-zinc

and zinc-nickel batteries;<sup>198–200</sup> however, many adverse side reactions exist between Zn electrodes and the electrolyte during the reaction process, such as electrode passivation, zinc dendrite growth and electrode distortion.<sup>201–203</sup> In particular, the growth of zinc dendrites is caused by the inhomogeneous deposition of Zn during the charging process,<sup>204</sup> which can cause drastic degradation of the coulomb efficiencies and capacities of the batteries. More seriously, the two electrodes of the battery will come into contact when the dendrites pierce the membrane of the battery, leading to internal short-circuiting and termination of the battery. Various approaches have been proposed to combat zinc dendrites, including electrolyte optimization,<sup>205</sup> electrode surface modification<sup>206</sup> and electrode structure design,<sup>207</sup> nevertheless, comprehensive criteria for evaluating the state of metal anodes in aqueous metal-NO<sub>2</sub><sup>-</sup>/NO<sub>3</sub><sup>-</sup> batteries are currently lacking. Thus, the behavior of metal anodes in aqueous metal-NO<sub>2</sub><sup>-</sup>/NO<sub>3</sub><sup>-</sup> batteries could be considered as a priority for future studies.

Apart from the influence of Zn, the robustness of metal-NO<sub>2</sub><sup>-</sup>/NO<sub>3</sub><sup>-</sup> batteries is also affected by the consumption of NO<sub>2</sub><sup>-</sup>/NO<sub>3</sub><sup>-</sup>. To overcome this issue, a continuously stirring flow system can be introduced with steady NO<sub>2</sub><sup>-</sup>/NO<sub>3</sub><sup>-</sup> concentration and stable current density. Future efforts can be attempted in the design and construction of highly efficient and selective electrocatalysts applied in a flow metal-NO<sub>2</sub><sup>-</sup>/NO<sub>3</sub><sup>-</sup> battery system.

In addition to enhancing the metal-NO<sub>2</sub><sup>-</sup>/NO<sub>3</sub><sup>-</sup> battery performance by optimizing electrode catalysts and metal anodes, some attempts have recently been made to replace the Zn oxidation reaction with other oxidation reactions including hydrazine (N<sub>2</sub>H<sub>4</sub>) oxidation. Theoretically, a battery can be



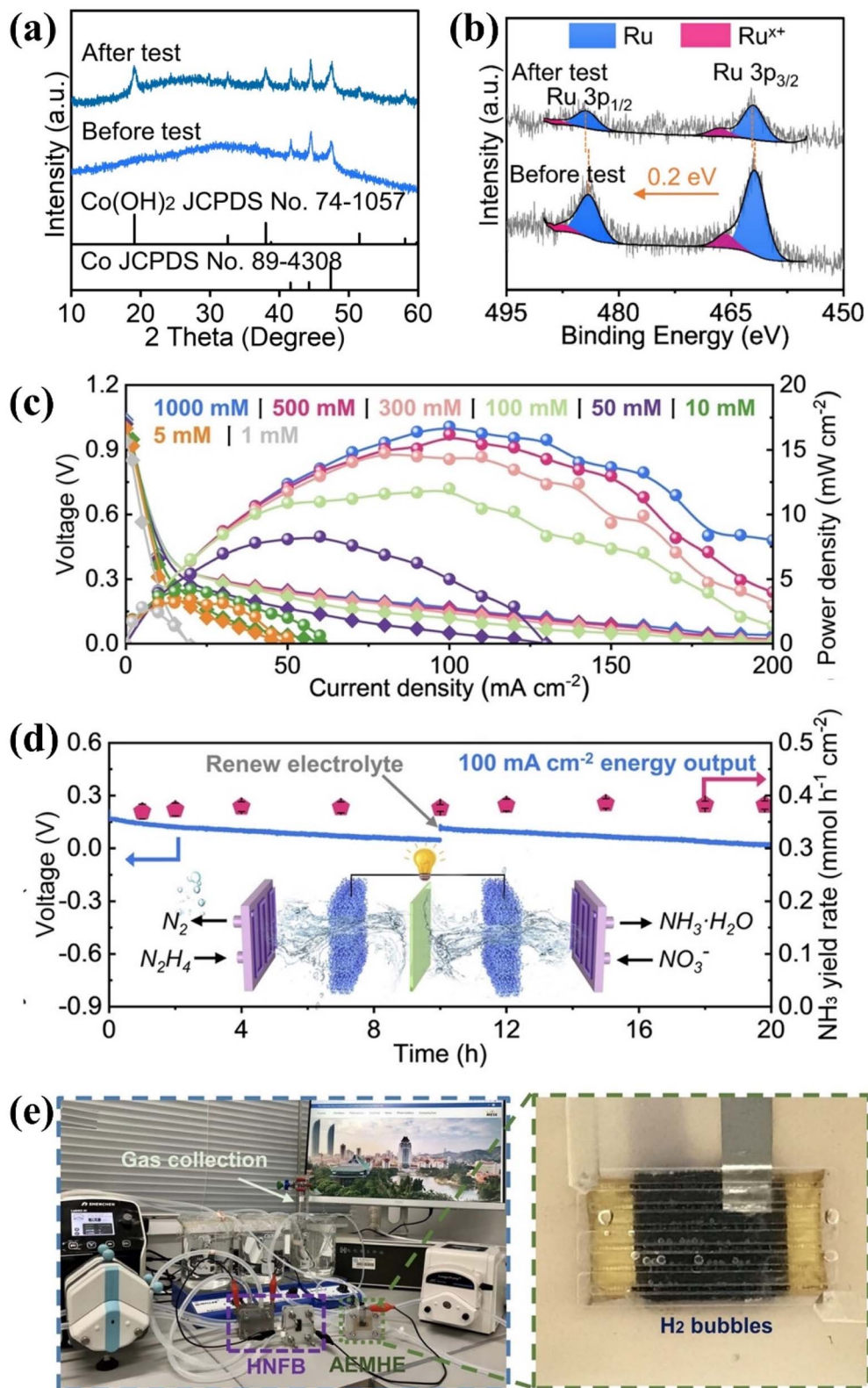


Fig. 13 (a) XRD pattern and (b) Ru 3p spectra of RuCo catalysts before and after testing. (c) Power density curves and (d) stability test of the  $\text{N}_2\text{H}_4\text{-NO}_3^-$  flow battery. (e) Digital photograph of the tandem  $\text{N}_2\text{H}_4\text{-NO}_3^-$  flow battery and hydrogen production electrolyzer. Reproduced with permission.<sup>178</sup> Copyright 2023, Wiley-VCH.



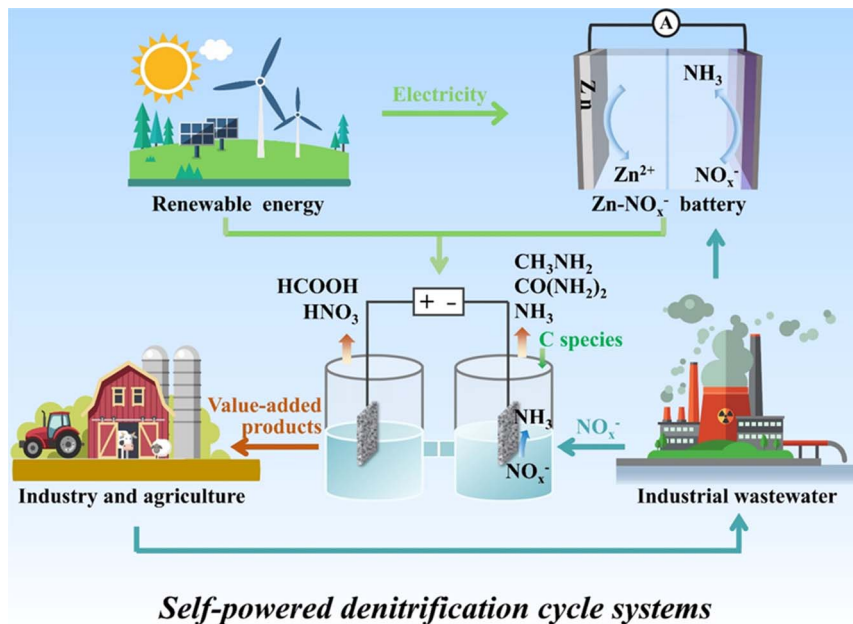


Fig. 14 The conceptual design of a self-powered denitrification system, which employs metal- $\text{NO}_x^-$  batteries storing intermittent energy to supply energy for treating wastewater and producing value-added chemicals by C-N coupling reactions and alternative anodic reactions based on electrocatalytic  $\text{NO}_x^-$  reduction.

composed of anodic  $\text{N}_2\text{H}_4$  oxidation to  $\text{N}_2$  and cathodic  $\text{NO}_3^-$  reduction to  $\text{NH}_3$ . In this battery, a high theoretical discharge voltage can be generated up to 1.04 V ( $\text{NO}_3^- + 2\text{N}_2\text{H}_4 \rightarrow \text{NH}_3 + 2\text{N}_2 + 2\text{H}_2\text{O} + \text{OH}^-$ ),<sup>208,209</sup> accompanied by sewage purification and  $\text{NH}_3$  production. Currently, in view of the importance of electrolyte renewal, a novel  $\text{N}_2\text{H}_4$ - $\text{NO}_3^-$  flow battery has been developed, which employs RuCo precatalysts as electrodes for accelerating both the  $\text{N}_2\text{H}_4$  oxidation and  $\text{NO}_3^-$  reduction.<sup>178</sup> The RuCo precatalysts have been confirmed to be reconstructed into Ru/Co(OH)<sub>2</sub> heterostructures during the electrocatalysis (Fig. 13a). The positive shift of 0.2 eV could be observed in the Ru 3p XPS peaks of the precatalyst after the test (Fig. 13b), suggesting the formation of electron-deficient Ru sites and strong interfacial interactions between Ru and Co(OH)<sub>2</sub>. The battery performances influenced by wastewater concentration are depicted in Fig. 13c. The discharge power density is gradually enhanced from 2.8 to 16.8  $\text{mW cm}^{-2}$  with the increase of concentration from 1 to 1000 mM. Fig. 13d illustrates the stability test of the  $\text{N}_2\text{H}_4$ - $\text{NO}_3^-$  flow battery in 0.1 M wastewater, which was operated continuously for 20 hours at 100  $\text{mA cm}^{-2}$  and maintains the  $\text{NH}_4$  production rate of roughly 0.38  $\text{mmol h}^{-1} \text{cm}^{-2}$ . In addition to the remarkable stability of Ru/Co(OH)<sub>2</sub> heterostructures, the lack of significant voltage degradation during the test may also be caused by the promotion of electrolyte renewal and recovery in the flow state. In addition, the promising potential of the  $\text{N}_2\text{H}_4$ - $\text{NO}_3^-$  flow battery has been demonstrated on electricity supply. As indicated in Fig. 13e, a low-voltage-driven anion exchange membrane hydrazine electrolyzer can be spontaneously driven by two tandem  $\text{N}_2\text{H}_4$ - $\text{NO}_3^-$  flow batteries, achieving a  $\text{H}_2$  production rate of 0.35  $\text{mmol h}^{-1} \text{cm}^{-2}$ , at output current density reaching 18.76  $\text{mA cm}^{-2}$ .

## 6. Summary and outlook

The electrocatalytic reduction of  $\text{NO}_x^-$  to ammonia has drawn renewed interest for the restoration of the nitrogen cycle and the promotion of ammonia-based economies. This paper reviews current studies of three valorization systems based on electrocatalytic  $\text{NO}_x^-$  conversion for energy supply and multifarious value-added chemicals synthesis, including waste treatment systems, novel electrolytic systems, and energy conversion and storage systems. In spite of the remarkable advances made in each application, some challenges and opportunities still exist.

### 6.1 Establishing uniform comparison standards and real experimental conditions

Uniform criteria are lacking in the field of  $\text{NO}_x^-$  reduction including benchmark materials, test conditions and ammonia production units, which can potentially misguide readers and peers in judging and comparing catalyst performance. In order to achieve comparison under similar conditions, a majority of efforts focus on creating an identical test environment by establishing analogous test conditions including the electrolyte pH,  $\text{NO}_3^-/\text{NO}_2^-$  concentration, and electrochemical test parameters such as applied potential and stability test duration. However, the pH,  $\text{NO}_x^-$  ion concentration and operating voltage in the electrolytic environment hardly remain constant for practical application situations. Most catalysts currently developed are primarily targeted at specific pH and  $\text{NO}_x^-$  ion concentration, ignoring the challenges of environments with variable pH,  $\text{NO}_x^-$  ion concentration and operating voltage. Therefore, electrodes are required to be developed which



generally exhibit remarkable FE and energy exchange efficiency over an extensive range of pH,  $\text{NO}_x^-$  ion concentration and electrode potentials. In addition, the effects of wastewater constituents on reaction activity and electrode fouling still need to be elucidated. For example, transition metal-based catalysts may be inactivated by complexing with interfering  $\text{SCN}^-$  ions in wastewater. Therefore, the effects of ionic strength, cation type, and competing anions should be thoroughly studied.

### 6.2 Deepening the mechanism research and improving the theoretical model

Although it is commonly recognized that the  $\text{NO}_3^-/\text{NO}_2^-$  reduction catalysts in alkaline environments are more inclined to exhibit higher FE and energy conversion efficiencies compared to those in other environments, the exploration of mechanisms in different environments is unclear. Currently, apart from the knowledge of excess  $\text{OH}^-$  ions inhibiting the HER, more intrinsic mechanisms have not been probed accompanied by the absence of reliable experimental evidence.

Moreover, in the majority of microkinetic models currently developed for screening efficient  $\text{NO}_x^-$  reduction catalysts, the microkinetic models are often simplified by assuming that  $N_{\text{ads}}$  is directly coupled to  $H_{\text{ads}}$ . However, this theoretical model only embodies the competition from the HER, but neglects the side reaction generating  $\text{N}_2$  and  $\text{NO}$ . A comprehensive competitive kinetic model that can adequately display the competition of  $\text{NO}_x^-$  reduction reactions, the HER and other side reactions generating N-containing species is currently lacking.

### 6.3 Optimizing product separation strategies

The current efforts on  $\text{NO}_x^-$  reduction to  $\text{NH}_3$  are mainly focused on enhancing the economic efficiency and reducing the energy consumption of  $\text{NH}_3$ , but the discussions on the subsequent  $\text{NH}_3$  separation are severely lacking. In electrochemical denitrification systems, the pH is constantly increased due to the consumption of  $\text{H}^+$  in the  $\text{NO}_x^-$  reduction process. The majority of  $\text{NH}_3$  produced at the electrolysis interface exists in the gaseous form. In addition to the traditional techniques separating  $\text{NH}_3$  including the air stripping method and extraction-condensation method, acid trapping and  $\text{CO}_2$  capture strategies have also been demonstrated to achieve  $\text{NH}_3$  separation, but the availability of pure  $\text{NH}_3$  using such strategies is facing safety risks and cost challenges. More reasonable separation strategies need to be developed with competitive cost.

### 6.4 Constructing self-powered denitrification systems

The current electrocatalytic reduction of  $\text{NO}_x^-$  to  $\text{NH}_3$  still relies on external electric power, posing a critical obstacle to practical applications in mobile devices. Therefore, a hypothetical integrated system called a “self-powered denitrification cycle system” is proposed, where  $\text{NO}_x^-$  reduction is powered by metal- $\text{NO}_x^-$  batteries storing intermittent renewable energies such as wind and solar energy. This hypothetical system (Fig. 14) can be coupled with the global nitrogen cycle, where high-value-added products based on  $\text{NO}_x^-$  reduction re-enter

the nitrogen cycle to provide abundant  $\text{NO}_x^-$  ions. The concept of self-powered denitrification cycle system not only opens up new insights for restoring the disturbed nitrogen cycle and boosting the nitrogen-based economy, but also provides a referable model for  $\text{NO}_x^-$  reduction in a realistic scenario.

The key to the successful construction of self-powered denitrification systems lies in the development of the ammonia economy. The flourishing of the ammonia economy is linked not only to advances in catalytic technology but also to the acceptance of ammonia as an energy source by the public and the promotion of ammonia by government policies.

The chemical conversion of other N species could be introduced into the self-powered denitrification cycle system based on  $\text{NO}_x^-$  reduction, which could further promote the restoration of the global N cycle and the prosperity of the N-based economy.  $\text{N}_2$ ,  $\text{NO}$  and  $\text{NO}_2$  could be converted to  $\text{NO}_x^-$ , providing a more stable approach for obtaining  $\text{NO}_x^-$  and high-value product  $\text{HNO}_3$ . Ammonia can be oxidized in various cells to provide hydrogen as a power source for denitrification systems.

### 6.5 From C–N coupling to artificial life synthesis

In order to enhance the efficiency and economic benefit of aqueous C–N coupling reactions and to broaden the range of N-containing organic products, it is crucial to promote the accumulation and generation of key N- and C-containing intermediates. A deeper knowledge of electrocatalytic reduction of individual organic molecules is required to genuinely facilitate the development of C–N coupling reactions.

More intriguingly, amino acid molecules have been confirmed to be formed by  $\text{CO}_2$  and  $\text{NO}_x^-$ . This corresponds to the first stage towards the origin of life, the evolution of inorganic molecules into organic substances in the primitive atmosphere and oceans, accompanied by energies from cosmic rays, lightning and volcanic explosion. Large accumulation of amino acid molecules could form primitive biomolecule proteins in the early oceans, and proteins could promote the process of dehydration and condensation of nucleic acids to form deoxyribonucleic acid (DNA). Subsequently, biomolecules evolved into multimolecular systems through condensation and polymerization. Finally, the organic polymolecular system evolves into primitive life, completing the intricate and lengthy process of gradual evolution from simple inorganic molecules into primitive life forms with self-replicating functions. The success of synthetic amino acids is of great importance for exploring the origin of life; moreover, with the reduction of electricity price and the development of alternative energy sources, artificial life synthesis and accelerated evolution of life is on the horizon using  $\text{CO}_2$ , N-containing substances and  $\text{H}_2\text{O}$ .

## Data availability

The datasets used and/or analyzed during the present study are available from the corresponding author upon reasonable request.



## Author contributions

Yi Feng: conceptualization, writing – original draft, writing – review & editing; Jin-Tao Ren: writing – review & editing; Ming-Lei Sun: writing – review & editing; Zhong-Yong Yuan: conceptualization, writing – review & editing, supervision.

## Conflicts of interest

The authors declare no conflict of interest.

## Acknowledgements

This work was supported by the National Natural Science Foundation of China (22179065, 22105108).

## References

- X. Fu, J. B. Pedersen, Y. Zhou, M. Saccoccio, S. Li, R. Sažinas, K. Li, S. Z. Andersen, A. Xu, N. H. Deissler, J. B. V. Mygind, C. Wei, J. Kibsgaard, P. C. K. Vesborg, J. K. Nørskov and I. Chorkendorff, *Science*, 2023, **379**, 707.
- P. H. van Langevelde, I. Katsounaros and M. T. M. Koper, *Joule*, 2021, **5**, 290.
- H. Wang, J. Ren, M. Sun, W. Tian, Y. Feng and Z. Yuan, *Adv. Energy Mater.*, 2024, **14**, 2302515.
- H. Luo, S. Li, Z. Wu, M. Jiang, M. Kuang, Y. Liu, W. Luo, D. Zhang and J. Yang, *Adv. Funct. Mater.*, 2024, **34**, 2403838.
- K. Wang, R. Mao, R. Liu, J. Zhang, H. Zhao, W. Ran and X. Zhao, *Nat. Mater.*, 2023, **1**, 1068.
- H. Xu, Y. Ma, J. Chen, W. X. Zhang and J. Yang, *Chem. Soc. Rev.*, 2022, **51**, 2710.
- M. Sun, H. Wang, Y. Feng, J. Ren, L. Wang and Z. Yuan, *Chem. Soc. Rev.*, 2024, DOI: [10.1039/d4cs00517a](https://doi.org/10.1039/d4cs00517a).
- Z. Wu, M. Karamad, X. Yong, Q. Huang, D. A. Cullen, P. Zhu, C. Xia, Q. Xiao, M. Shakouri, F. Chen, J. Y. T. Kim, Y. Xia, K. Heck, Y. Hu, M. S. Wong, Q. Li, I. Gates, S. Siahrostami and H. Wang, *Nat. Commun.*, 2021, **12**, 2870.
- D. R. Macfarlane, P. V. Cherepanov, J. Choi, B. H. R. Suryanto, R. Y. Hodgetts, J. M. Bakker, F. M. Ferrero Vallana and A. N. Simonov, *Joule*, 2020, **4**, 1186.
- Y. Pang and J. Wang, *Sci. Total Environ.*, 2021, **794**, 148699.
- X. Zou, J. Xie, C. Wang, G. Jiang, K. Tang and C. Chen, *Chin. Chem. Lett.*, 2022, **34**, 107908.
- J. Li, G. Zhan, J. Yang, F. Quan, C. Mao, Y. Liu, B. Wang, F. Lei, L. Li, A. W. M. Chan, L. Xu, Y. Shi, Y. Du, W. Hao, P. K. Wong, J. Wang, S. Dou, L. Zhang and J. C. Yu, *J. Am. Chem. Soc.*, 2020, **142**, 7036.
- X. Fan, X. He, X. Ji, L. Zhang, J. Li, L. Hu, X. Li, S. Sun, D. Zheng, Y. Luo, Y. Wang, L. Xie, Q. Liu, B. Ying and X. Sun, *Inorg. Chem. Front.*, 2023, **10**, 1431–1435.
- P. Gao, Z. Xue, S. Zhang, D. Xu, G. Zhai, Q. Li, J. Chen and X. Li, *Angew. Chem., Int. Ed.*, 2021, **60**, 20711.
- R. Li, W. Ma, Y. Liu, L. Zhang and Z. Zhou, *J. Mater. Chem. A*, 2023, **11**, 18626–18645.
- J. Lim, C. A. Fernández, S. W. Lee and M. C. Hatzell, *ACS Energy Lett.*, 2021, **6**, 3676.
- C. Wang, Y. Zhang, H. Luo, H. Zhang, W. Li, W. X. Zhang and J. Yang, *Small Methods*, 2022, **6**, 2200790.
- X. Lv, Y. Liu, Y. Wang, X. Liu and Z. Yuan, *Appl. Catal., B*, 2021, **280**, 119434.
- J. Shi, C. Wang, R. Yang, F. Chen, N. Meng, Y. Yu and B. Zhang, *Sci. China:Chem.*, 2021, **64**, 1493.
- X. Lv, X. Liu, Y. Suo, Y. Liu and Z. Yuan, *ACS Nano*, 2021, **15**, 12109.
- X. Zhang, A. Chen, L. Chen and Z. Zhou, *Adv. Energy Mater.*, 2022, **12**, 2003841.
- Z. Li, J. Liang, Q. Liu, L. Xie, L. Zhang, Y. Ren, L. Yue, N. Li, B. Tang, A. A. Alshehri, M. S. Hamdy, Y. Luo, Q. Kong and X. Sun, *Mater. Today Phys.*, 2022, **23**, 100619.
- R. Zhang, S. Zhang, Y. Guo, C. Li, J. Liu, Z. Huang, Y. Zhao, Y. Li and C. Zhi, *Energy Environ. Sci.*, 2022, **15**, 3024.
- W. Tian, Y. Ying, J. Ren and Z. Yuan, *J. Mater. Chem. A*, 2023, **11**, 8024.
- J. Ren, L. Chen, L. Wang, X. Song, Q. Kong and Z. Yuan, *J. Mater. Chem. A*, 2023, **11**, 2899.
- J. Qu, Z. Wang, W. Gan, R. Xiao, X. Yao, Z. Khanam, L. Ouyang, H. Wang, H. Yang, S. Zhang and M. Balogun, *Small*, 2024, **20**, 2304541.
- R. Yang, X. Zheng, M. Qin, B. Lin, X. Shi and Y. Wang, *Adv. Sci.*, 2022, **9**, 2201594.
- S. Liu, S. Yin, Z. Wang, Y. Xu, X. Li, L. Wang and H. Wang, *Cell Rep. Phys. Sci.*, 2022, **3**, 100869.
- Y. Wu, Z. Jiang, Z. Lin, Y. Liang and H. Wang, *Nat. Sustain.*, 2021, **4**, 725.
- T. Ren, Z. Yu, H. Yu, K. Deng, Z. Wang, X. Li, H. Wang, L. Wang and Y. Xu, *ACS Nano*, 2023, **17**, 12422.
- L. Xiao, W. Dai, S. Mou, X. Wang, Q. Cheng and F. Dong, *Energy Environ. Sci.*, 2023, **16**, 2696.
- X. Zhang, Y. Wang, C. Liu, Y. Yu, S. Lu and B. Zhang, *Chem. Eng. J.*, 2021, **403**, 126269.
- J. Liu, D. Richards, N. Singh and B. R. Goldsmith, *ACS Catal.*, 2019, **9**, 7052.
- Y. Wang, C. Wang, M. Li, Y. Yu and B. Zhang, *Chem. Soc. Rev.*, 2021, **50**, 6720.
- J. Theerthagiri, J. Park, H. T. Das, N. Rahamathulla, E. S. F. Cardoso, A. P. Murthy, G. Maia, D. V. N. Vo and M. Y. Choi, *Environ. Chem. Lett.*, 2022, **20**, 2929.
- R. Jia, Y. Wang, C. Wang, Y. Ling, Y. Yu and B. Zhang, *ACS Catal.*, 2020, **10**, 3533.
- J. Long, S. Chen, Y. Zhang, C. Guo, X. Fu, D. Deng and J. Xiao, *Angew. Chem., Int. Ed.*, 2020, **59**, 9711.
- X. Lan, C. Cheng, C. Guo, M. Guo, T. Li, Y. Wu, Y. Yu and B. Zhang, *Sci. China:Chem.*, 2023, **66**, 1758.
- C. Wang, Y. Zhang, H. Luo, H. Zhang, W. Li, W. Zhang and J. Yang, *Small Methods*, 2022, **6**, 2200790.
- Z. Deng, J. Liang, Q. Liu, C. Ma, L. Xie, L. Yue, Y. Ren, T. Li, Y. Luo, N. Li, B. Tang, A. Ali Alshehri, I. Shakir, P. O. Agboola, S. Yan, B. Zheng, J. Du, Q. Kong and X. Sun, *Chem. Eng. J.*, 2022, **435**, 135104.
- L. Xie, Q. Liu, S. Sun, L. Hu, L. Zhang, D. Zhao, Q. Liu, J. Chen, J. Li, L. Ouyang, A. A. Alshehri, M. S. Hamdy,



- Q. Kong and X. Sun, *ACS Appl. Mater. Interfaces*, 2022, **14**, 33242.
- 42 W. Chen, X. Yang, Z. Chen, Z. Ou, J. Hu, Y. Xu, Y. Li, X. Ren, S. Ye, J. Qiu, J. Liu and Q. Zhang, *Adv. Funct. Mater.*, 2023, **33**, 2300512.
- 43 H. Jiang, G. Chen, O. Savateev, J. Xue, L. Ding, Z. Liang, M. Antonietti and H. Wang, *Angew. Chem., Int. Ed.*, 2023, **62**, 202218717.
- 44 A. Khorshidi, J. Violet, J. Hashemi and A. A. Peterson, *Nat. Catal.*, 2018, **1**, 263.
- 45 J. Pérez-Ramírez and N. López, *Nat. Catal.*, 2019, **2**, 971.
- 46 M. Zhang, K. Zhang, X. Ai, X. Liang, Q. Zhang, H. Chen and X. Zou, *Chin. J. Catal.*, 2022, **43**, 2987.
- 47 Z. Zhao, S. Liu, S. Zha, D. Cheng, F. Studt, G. Henkelman and J. Gong, *Nat. Rev. Mater.*, 2019, **4**, 792.
- 48 Q. Gao, H. S. Pillai, Y. Huang, S. Liu, Q. Mu, X. Han, Z. Yan, H. Zhou, Q. He, H. Xin and H. Zhu, *Nat. Commun.*, 2022, **13**, 2338.
- 49 Y. Zhou, R. Duan, H. Li, M. Zhao, C. Ding and C. Li, *ACS Catal.*, 2023, **13**, 10846.
- 50 S. Ma and Z. Liu, *ACS Catal.*, 2020, **10**, 13213.
- 51 L. Chen, X. Zhang, A. Chen, S. Yao, X. Hu and Z. Zhou, *Chin. J. Catal.*, 2022, **43**, 11.
- 52 W. Ma, S. Xie, T. Liu, Q. Fan, J. Ye, F. Sun, Z. Jiang, Q. Zhang, J. Cheng and Y. Wang, *Nat. Catal.*, 2020, **3**, 478.
- 53 K. Fan, W. Xie, J. Li, Y. Sun, P. Xu, Y. Tang, Z. Li and M. Shao, *Nat. Commun.*, 2022, **13**, 7958.
- 54 Y. Wang, A. Xu, Z. Wang, L. Huang, J. Li, F. Li, J. Wicks, M. Luo, D. Nam, C. Tan, Y. Ding, J. Wu, Y. Lum, C. Dinh, D. Sinton, G. Zheng and E. H. Sargent, *J. Am. Chem. Soc.*, 2020, **142**, 5702.
- 55 H. Xu, Y. Ma, J. Chen, W. Zhang and J. Yang, *Chem. Soc. Rev.*, 2022, **51**, 2710.
- 56 J. Liu, H. Xiao and J. Li, *J. Am. Chem. Soc.*, 2020, **142**, 3375.
- 57 Q. Gao, B. Yao, H. S. Pillai, W. Zang, X. Han, Y. Liu, S. Yu, Z. Yan, B. Min, S. Zhang, H. Zhou, L. Ma, H. Xin, Q. He and H. Zhu, *Nat. Synth.*, 2023, **2**, 624.
- 58 J. Zhou, M. Wen, R. Huang, Q. Wu, Y. Luo, Y. Tian, G. Wei and Y. Fu, *Energy Environ. Sci.*, 2023, **16**, 2611.
- 59 Z. Fang, Z. Jin, S. Tang, P. Li, P. Wu and G. Yu, *ACS Nano*, 2022, **16**, 1072–1081.
- 60 J. Yu, Y. Qin, X. Wang, H. Zheng, K. Gao, H. Yang, L. Xie, Q. Hu and C. He, *Nano Energy*, 2022, **103**, 107705.
- 61 A. Angulo, P. van der Linde, H. Gardeniers, M. Modestino and D. Fernández Rivas, *Joule*, 2020, **4**, 555.
- 62 S. Zhang, J. Wu, M. Zheng, X. Jin, Z. Shen, Z. Li, Y. Wang, Q. Wang, X. Wang, H. Wei, J. Zhang, P. Wang, S. Zhang, L. Yu, L. Dong, Q. Zhu, H. Zhang and J. Lu, *Nat. Commun.*, 2023, **14**, 3634.
- 63 L. Wang, L. Zhang, W. Ma, H. Wan, X. Zhang, X. Zhang, S. Jiang, J. Y. Zheng and Z. Zhou, *Adv. Funct. Mater.*, 2022, **32**, 2203342.
- 64 Y. Xue, Q. Yu, Q. Ma, Y. Chen, C. Zhang, W. Teng, J. Fan and W. Zhang, *Environ. Sci. Technol.*, 2022, **56**, 14797.
- 65 Y. Zhang, X. Chen, W. Wang, L. Yin and J. C. Crittenden, *Appl. Catal., B*, 2022, **310**, 121346.
- 66 H. Liu, X. Lang, C. Zhu, J. Timoshenko, M. Rüscher, L. Bai, N. Guijarro, H. Yin, Y. Peng, J. Li, Z. Liu, W. Wang, B. R. Cuenya and J. Luo, *Angew. Chem., Int. Ed.*, 2022, **61**, 202202556.
- 67 J. Wang, C. Liang, X. Ma, P. Liu, W. Pan, H. Zhu, Z. Guo, Y. Sui, H. Liu, L. Liu and C. Yang, *Adv. Mater.*, 2023, **45**, 2307925.
- 68 H. Liu, X. Li, L. Chen, X. Zhu, P. Dong, M. O. L. Chee, M. Ye, Y. Guo and J. Shen, *Adv. Funct. Mater.*, 2022, **32**, 2107308.
- 69 Y. Xu, H. Liang, R. Li, Z. Zhang, C. Qin, D. Xu, H. Fan, B. Hou, J. Wang, X. Gu and M. Ding, *Angew. Chem., Int. Ed.*, 2023, **62**, 202306786.
- 70 Y. Feng, J. Ren, Y. Song, W. Tian, H. Wang, L. Wang, M. Sun and Z. Yuan, *CCS Chem.*, 2024, DOI: [10.31635/ccschem.024.202404299](https://doi.org/10.31635/ccschem.024.202404299).
- 71 C. Weng, X. Lv, J. Ren, T. Ma and Z. Yuan, *Electrochem. Energy Rev.*, 2022, **5**, 19.
- 72 W. Xu, Z. Lu, X. Sun, L. Jiang and X. Duan, *Acc. Chem. Res.*, 2018, **51**, 1590.
- 73 G. Liu, W. S. Y. Wong, M. Kraft, J. W. Ager, D. Vollmer and R. Xu, *Chem. Soc. Rev.*, 2021, **50**, 10674.
- 74 S. Garcia-Segura, M. Lanzarini-Lopes, K. Hristovski and P. Westerhoff, *Appl. Catal., B*, 2018, **236**, 546.
- 75 Y. Zhong, H. Xiong, J. Low, R. Long and Y. Xiong, *eScience*, 2023, **3**, 100086.
- 76 J. M. Mccanney, S. J. Blair, A. C. Nielander, J. A. Schwalbe, D. M. Koshy, M. Cargnello and T. F. Jaramillo, *ACS Sustain. Chem. Eng.*, 2020, **8**, 2672.
- 77 I. Katsounaros, *Curr. Opin. Electrochem.*, 2021, **28**, 100721.
- 78 Y. Bu, C. Wang, W. Zhang, X. Yang, J. Ding and G. Gao, *Angew. Chem., Int. Ed.*, 2023, **62**, 202217337.
- 79 J. Gao, B. Jiang, C. Ni, Y. Qi, Y. Zhang, N. Oturan and M. A. Oturan, *Appl. Catal., B*, 2019, **254**, 391.
- 80 J. Wang, Y. Wang, C. Cai, Y. Liu, D. Wu, M. Wang, M. Li, X. Wei, M. Shao and M. Gu, *Nano Lett.*, 2023, **23**, 1897.
- 81 C. Zhong, B. Liu, J. Ding, X. Liu, Y. Zhong, Y. Li, C. Sun, X. Han, Y. Deng, N. Zhao and W. Hu, *Nat. Energy*, 2020, **5**, 440.
- 82 Z. Wenxiao, Z. Liuyi, Y. Zhang, L. Zichao, L. Zhenchao, Z. Yifan, X. Haolin, D. Zhi, W. Chaohai and F. Chunhua, *Environ. Sci. Technol.*, 2021, **55**, 13231.
- 83 Z. Xu, L. Wan, Y. Liao, M. Pang, Q. Xu, P. Wang and B. Wang, *Nat. Commun.*, 2023, **14**, 1619.
- 84 C. Chen, X. Zhu, X. Wen, Y. Zhou, L. Zhou, H. Li, L. Tao, Q. Li, S. Du, T. Liu, D. Yan, C. Xie, Y. Zou, Y. Wang, R. Chen, J. Huo, Y. Li, J. Cheng, H. Su, X. Zhao, W. Cheng, Q. Liu, H. Lin, J. Luo, J. Chen, M. Dong, K. Cheng, C. Li and S. Wang, *Nat. Chem.*, 2020, **12**, 717.
- 85 J. Lv, M. Jouny, W. Luc, W. Zhu, J. Zhu and F. Jiao, *Adv. Mater.*, 2018, **30**, 1803111.
- 86 F. Li, A. Thevenon, A. Rosas-Hernández, Z. Wang, Y. Li, C. M. Gabardo, A. Ozden, C. T. Dinh, J. Li, Y. Wang, J. P. Edwards, Y. Xu, C. Mccallum, L. Tao, Z. Liang, M. Luo, X. Wang, H. Li, C. P. O'Brien, C. Tan, D. Nam, R. Quintero-Bermudez, T. Zhuang, Y. C. Li, Z. Han, R. D. Britt, D. Sinton, T. Agapie, J. C. Peters and E. H. Sargent, *Nature*, 2020, **577**, 509.



- 87 Y. Zeng, C. Priest, G. Wang and G. Wu, *Small Methods*, 2020, **4**, 2000672.
- 88 Z. Wu, Y. Song, Y. Liu, W. Luo, W. Li and J. Yang, *Chem Catal.*, 2023, **3**, 100786.
- 89 Y. Liu, M. Chen, X. Zhao, H. Zhang, Y. Zhao and Y. Zhou, *Chem. Eng. J.*, 2023, **475**, 146176.
- 90 H. Xu, J. Chen, Z. Zhang, C. Hung, J. Yang and W. Li, *Adv. Mater.*, 2023, **35**, 2207522.
- 91 J. Sun, H. Yang, W. Gao, T. Cao and G. Zhao, *Angew. Chem., Int. Ed.*, 2022, **61**, 202211373.
- 92 H. Huang, K. Peramaiah and K. Huang, *Energy Environ. Sci.*, 2024, **17**, 2682–2685.
- 93 C. Fu, S. Shu, L. Hu, Z. Liu, Z. Yin, X. Lv, S. Zhang and G. Jiang, *Chem. Eng. J.*, 2022, **435**, 134969.
- 94 X. Wang, M. Zhu, G. Zeng, X. Liu, C. Fang and C. Li, *Nanoscale*, 2020, **12**, 9385.
- 95 F. Ni, Y. Ma, J. Chen, W. Luo and J. Yang, *Chin. Chem. Lett.*, 2021, **32**, 2073.
- 96 L. Su, K. Li, H. Zhang, M. Fan, D. Ying, T. Sun, Y. Wang and J. Jia, *Water Res.*, 2017, **120**, 1.
- 97 R. Chauhan and V. C. Srivastava, *Chem. Eng. J.*, 2020, **386**, 122065.
- 98 T. T. P. Nguyen, B. K. D. Do, N. N. Bui, M. A. Pham and T. V. Nguyen, *ECS Trans.*, 2013, **53**, 41.
- 99 I. Katsounaros, M. Dortsiou and G. Kyriacou, *J. Hazard. Mater.*, 2009, **171**, 323.
- 100 G. Chen, Y. Yuan, H. Jiang, S. Ren, L. Ding, L. Ma, T. Wu, J. Lu and H. Wang, *Nat. Energy*, 2020, **5**, 605.
- 101 T. F. Beltrame, D. Carvalho, L. Marder, M. A. Ulla, F. A. Marchesini and A. M. Bernardes, *J. Environ. Chem. Eng.*, 2020, **8**, 104120.
- 102 Y. Zeng, C. Priest, G. Wang and G. Wu, *Small Methods*, 2020, **4**, 2000672.
- 103 G. Jiang, M. Peng, L. Hu, J. Ouyang, X. Lv, Z. Yang, X. Liang, Y. Liu and H. Liu, *Chem. Eng. J.*, 2022, **435**, 134853.
- 104 I. Katsounaros and G. Kyriacou, *Electrochim. Acta*, 2007, **52**, 6412.
- 105 S. Meng, Y. Ling, M. Yang, X. Zhao, A. I. Osman, A. A. H. Al-Muhtaseb, D. W. Rooney and P. Yap, *J. Environ. Chem. Eng.*, 2023, **11**, 109418.
- 106 J. Makover, D. Hasson, R. Semiat and H. Shemer, *J. Environ. Chem. Eng.*, 2020, **8**, 103727.
- 107 M. J. Liu, D. M. Miller and W. A. Tarpeh, *Environ. Sci. Technol. Lett.*, 2023, **10**, 458.
- 108 S. L. Foster, S. I. P. Bakovic, R. D. Duda, S. Maheshwari, R. D. Milton, S. D. Minter, M. J. Janik, J. N. Renner and L. F. Greenlee, *Nat. Catal.*, 2018, **1**, 490.
- 109 B. H. Ko, B. Hasa, H. Shin, Y. Zhao and F. Jiao, *J. Am. Chem. Soc.*, 2022, **144**, 1258.
- 110 X. Deng, Y. Yang, L. Wang, X. Fu and J. Luo, *Adv. Sci.*, 2021, **8**, 2004523.
- 111 Q. Hu, K. Yang, O. Peng, M. Li, L. Ma, S. Huang, Y. Du, Z. Xu, Q. Wang, Z. Chen, M. Yang and K. P. Loh, *J. Am. Chem. Soc.*, 2024, **146**, 668.
- 112 O. Q. Carvalho, R. Marks, H. K. K. Nguyen, M. E. Vitale-Sullivan, S. C. Martinez, L. árнадóttir and K. A. Stoerzinger, *J. Am. Chem. Soc.*, 2022, **144**, 14809.
- 113 W. Zhong, Q. Hong, X. Ai, C. Zhang, F. Li, X. Li and Y. Chen, *Adv. Mater.*, 2024, **46**, 2314351.
- 114 Y. Lv, S. Ke, Y. Gu, B. Tian, L. Tang, P. Ran, Y. Zhao, J. Ma, J. Zuo and M. Ding, *Angew. Chem., Int. Ed.*, 2023, **62**, 202305246.
- 115 H. Zhang, C. Wang, H. Luo, J. Chen, M. Kuang and J. Yang, *Angew. Chem., Int. Ed.*, 2023, **62**, e202217071.
- 116 Y. Feng, L. Chen and Z. Yuan, *Inorg. Chem. Front.*, 2023, **10**, 5225.
- 117 K. Yu, H. Wang, W. Yu, S. Li, X. Zhang and Z. Bian, *Appl. Catal., B*, 2024, **341**, 123292.
- 118 C. Tang, Y. Zheng, M. Jaroniec and S. Qiao, *Angew. Chem., Int. Ed.*, 2021, **60**, 19572.
- 119 J. Liang, Z. Li, L. Zhang, X. He, Y. Luo, D. Zheng, Y. Wang, T. Li, H. Yan, B. Ying, S. Sun, Q. Liu, M. S. Hamdy, B. Tang and X. Sun, *Chem*, 2023, **9**, 1768.
- 120 S. Ye, Z. Chen, G. Zhang, W. Chen, C. Peng, X. Yang, L. Zheng, Y. Li, X. Ren, H. Cao, D. Xue, J. Qiu, Q. Zhang and J. Liu, *Energy Environ. Sci.*, 2022, **15**, 760.
- 121 C. Wang, W. Zhou, Z. Sun, Y. Wang, B. Zhang and Y. Yu, *J. Mater. Chem. A*, 2021, **9**, 239.
- 122 W. R. Leow, Y. Lum, A. Ozden, Y. Wang, D. Nam, B. Chen, J. Wicks, T. Zhuang, F. Li, D. Sinton and E. H. Sargent, *Science*, 2020, **368**, 1228.
- 123 Y. Zhang, Y. Wang, L. Han, S. Wang, T. Cui, Y. Yan, M. Xu, H. Duan, Y. Kuang and X. Sun, *Angew. Chem., Int. Ed.*, 2022, **61**, 202213711.
- 124 Z. Mei, Y. Zhou, W. Lv, S. Tong, X. Yang, L. Chen and N. Zhang, *ACS Sustain. Chem. Eng.*, 2022, **10**, 12477.
- 125 J. Leverett, T. Tran Phu, J. A. Yuwono, P. Kumar, C. Kim, Q. Zhai, C. Han, J. Qu, J. Cairney, A. N. Simonov, R. K. Hocking, L. Dai, R. Daiyan and R. Amal, *Adv. Energy Mater.*, 2022, **12**, 2201500.
- 126 Z. Tao, C. L. Rooney, Y. Liang and H. Wang, *J. Am. Chem. Soc.*, 2021, **143**, 19630.
- 127 N. Meng, Y. Huang, Y. Liu, Y. Yu and B. Zhang, *Cell Rep. Phys. Sci.*, 2021, **2**, 100378.
- 128 C. Lv, L. Zhong, H. Liu, Z. Fang, C. Yan, M. Chen, Y. Kong, C. Lee, D. Liu, S. Li, J. Liu, L. Song, G. Chen, Q. Yan and G. Yu, *Nat. Sustain.*, 2021, **4**, 868.
- 129 Y. Liu, X. Tu, X. Wei, D. Wang, X. Zhang, W. Chen, C. Chen and S. Wang, *Angew. Chem., Int. Ed.*, 2023, **62**, 202300387.
- 130 S. Liu, M. Wang, Q. Cheng, Y. He, J. Ni, J. Liu, C. Yan and T. Qian, *ACS Nano*, 2022, **16**, 17911.
- 131 Y. Luo, K. Xie, P. Ou, C. Lavallais, T. Peng, Z. Chen, Z. Zhang, N. Wang, X. Li, I. Grigioni, B. Liu, D. Sinton, J. B. Dunn and E. H. Sargent, *Nat. Catal.*, 2023, **6**, 939–948.
- 132 X. Huang, Y. Li, S. Xie, Q. Zhao, B. Zhang, Z. Zhang, H. Sheng and J. Zhao, *Angew. Chem., Int. Ed.*, 2024, **63**, 202403980.
- 133 Y. Feng, L. Chen and Z. Yuan, *J. Ind. Eng. Chem.*, 2023, **120**, 27.
- 134 A. V. Munde, B. B. Mulik, R. P. Dighole and B. R. Sathe, *ACS Appl. Energy Mater.*, 2021, **4**, 13172.
- 135 N. Meng, X. Ma, C. Wang, Y. Wang, R. Yang, J. Shao, Y. Huang, Y. Xu, B. Zhang and Y. Yu, *ACS Nano*, 2022, **16**, 9095.



- 136 Y. Feng, H. Yang, Y. Zhang, X. Huang, L. Li, T. Cheng and Q. Shao, *Nano Lett.*, 2020, **20**, 8282.
- 137 X. Lv, Y. Liu, R. Hao, W. Tian and Z. Yuan, *ACS Appl. Mater. Interfaces*, 2020, **12**, 17502.
- 138 N. Cao, Y. Quan, A. Guan, C. Yang, Y. Ji, L. Zhang and G. Zheng, *J. Colloid Interface Sci.*, 2020, **577**, 109.
- 139 Q. Zhang and J. Guan, *Nano Res.*, 2022, **15**, 38.
- 140 J. Leverett, T. Tran-Phu, J. A. Yuwono, P. Kumar, C. Kim, Q. Zhai, C. Han, J. Qu, J. Cairney, A. N. Simonov, R. K. Hocking, L. Dai, R. Daiyan and R. Amal, *Adv. Energy Mater.*, 2022, **12**, 2201500.
- 141 X. Zhang, X. Zhu, S. Bo, C. Chen, M. Qiu, X. Wei, N. He, C. Xie, W. Chen, J. Zheng, P. Chen, S. P. Jiang, Y. Li, Q. Liu and S. Wang, *Nat. Commun.*, 2022, **13**, 5337.
- 142 L. Chen and Z. Yuan, *J. Ind. Eng. Chem.*, 2022, **108**, 1.
- 143 X. Liu, P. V. Kumar, Q. Chen, L. Zhao, F. Ye, X. Ma, D. Liu, X. Chen, L. Dai and C. Hu, *Appl. Catal., B*, 2022, **316**, 121618.
- 144 C. Hu, Y. Lin, J. W. Connell, H. Cheng, Y. Gogotsi, M. Titirici and L. Dai, *Adv. Mater.*, 2019, **31**, 1806128.
- 145 C. Chen, S. Li, X. Zhu, S. Bo, K. Cheng, N. He, M. Qiu, C. Xie, D. Song, Y. Liu, W. Chen, Y. Li, Q. Liu, C. Li and S. Wang, *Carbon Energy*, 2023, **5**, 345.
- 146 Y. Huan, Y. Jiang, L. Li, Y. He, Q. Cheng, Y. Cao, M. Wang, C. Yan and T. Qian, *ACS Mater. Lett.*, 2023, **5**, 3347.
- 147 J. Liang, Z. Cai, Z. Li, Y. Yao, Y. Luo, S. Sun, D. Zheng, Q. Liu, X. Sun and B. Tang, *Nat. Commun.*, 2024, **15**, 2950.
- 148 J. Li and N. Kornienko, *Chem. Sci.*, 2022, **13**, 3957.
- 149 M. Jouny, J. Lv, T. Cheng, B. H. Ko, J. Zhu, W. A. Goddard and F. Jiao, *Nat. Chem.*, 2019, **11**, 846.
- 150 J. Lan, Z. Wei, Y. Lu, D. Chen, S. Zhao, T. Chan and Y. Tan, *Nat. Commun.*, 2023, **14**, 2870.
- 151 N. Meng, J. Shao, H. Li, Y. Wang, X. Fu, C. Liu, Y. Yu and B. Zhang, *Nat. Commun.*, 2022, **13**, 5452.
- 152 J. Shao, N. Meng, Y. Wang, B. Zhang, K. Yang, C. Liu, Y. Yu and B. Zhang, *Angew. Chem., Int. Ed.*, 2022, **61**, 202213009.
- 153 Z. Tao, Y. Wu, Z. Wu, B. Shang, C. Rooney and H. Wang, *J. Energy Chem.*, 2022, **65**, 367.
- 154 F. Rieck Genannt Best, A. Mundstock, H. Richter, P. A. Kießling, K. D. J. Hindricks, A. Huang, P. Behrens and J. Caro, *Microporous Mesoporous Mater.*, 2022, **337**, 111920.
- 155 Z. Tao, Y. Wu, Z. Wu, B. Shang, C. Rooney and H. Wang, *J. Energy Chem.*, 2022, **65**, 367.
- 156 M. He, Y. Wu, R. Li, Y. Wang, C. Liu and B. Zhang, *Nat. Commun.*, 2023, **14**, 5088.
- 157 J. Wu, L. Xu, Z. Kong, K. Gu, Y. Lu, X. Wu, Y. Zou and S. Wang, *Angew. Chem., Int. Ed.*, 2023, e202311196.
- 158 H. Yadegari, A. Ozden, T. Alkayali, V. Soni, A. Thevenon, A. Rosas-Hernández, T. Agapie, J. C. Peters, E. H. Sargent and D. Sinton, *ACS Energy Lett.*, 2021, **6**, 3538.
- 159 Y. Wang, Y. Yu, R. Jia, C. Zhang and B. Zhang, *Natl. Sci. Rev.*, 2019, **6**, 730.
- 160 H. Wang, L. Wang, J. Ren, W. Tian, M. Sun and Z. Yuan, *Nano-Micro Lett.*, 2023, **15**, 155.
- 161 J. Wu, L. Xu, Z. Kong, K. Gu, Y. Lu, X. Wu, Y. Zou and S. Wang, *Angew. Chem., Int. Ed.*, 2023, e202311196.
- 162 D. Li, Z. Li, R. Zou, G. Shi, Y. Huang, W. Yang, W. Yang, C. Liu and X. Peng, *Appl. Catal., B*, 2022, **307**, 121170.
- 163 J. Wu, J. Chen, T. Yu, Z. Zhai, Y. Zhu, X. Wu and S. Yin, *ACS Catal.*, 2023, **13**, 13257–13266.
- 164 R. Zhong, P. Wu, Q. Wang, X. Zhang, L. Du, Y. Liu, H. Yang, M. Gu, Z. C. Zhang, L. Huang and S. Ye, *Green Chem.*, 2023, **25**, 4674.
- 165 C. Huang, Y. Huang, C. Liu, Y. Yu and B. Zhang, *Angew. Chem., Int. Ed.*, 2019, **58**, 12014.
- 166 Y. Wu, C. Liu, C. Wang, Y. Yu, Y. Shi and B. Zhang, *Nat. Commun.*, 2021, **12**, 3881.
- 167 S. Li, P. Ma, C. Gao, L. Liu, X. Wang, M. Shakouri, R. Chernikov, K. Wang, D. Liu, R. Ma and J. Wang, *Energy Environ. Sci.*, 2022, **15**, 3004.
- 168 J. Li, H. Li, K. Fan, J. Y. Lee, W. Xie and M. Shao, *Chem Catal.*, 2023, **3**, 100638.
- 169 Z. Li, Y. Yan, S. Xu, H. Zhou, M. Xu, L. Ma, M. Shao, X. Kong, B. Wang and L. Zheng, *Nat. Commun.*, 2022, **13**, 147.
- 170 Z. Yin, Y. Zheng, H. Wang, J. Li, Q. Zhu, Y. Wang, N. Ma, G. Hu, B. He, A. Knop-Gericke, R. Schlögl and D. Ma, *ACS Nano*, 2017, **11**, 12365.
- 171 H. Huang, C. Yu, X. Han, H. Huang, Q. Wei, W. Guo, Z. Wang and J. Qiu, *Energy Environ. Sci.*, 2021, **14**, 6055.
- 172 M. Axelsson, C. F. Marchiori, P. Huang, C. M. Araujo and H. Tian, *J. Am. Chem. Soc.*, 2021, **143**, 21229.
- 173 H. Zhou, Z. Li, S. Xu, L. Lu, M. Xu, K. Ji, R. Ge, Y. Yan, L. Ma, X. Kong, L. Zheng and H. Duan, *Angew. Chem., Int. Ed.*, 2021, **60**, 8976.
- 174 Z. Chen, J. Dong, J. Wu, Q. Shao, N. Luo, M. Xu, Y. Sun, Y. Tang, J. Peng and H. Cheng, *Nat. Commun.*, 2023, **14**, 4210.
- 175 Q. Liu, L. Xie, J. Liang, Y. Ren, Y. Wang, L. Zhang, L. Yue, T. Li, Y. Luo, N. Li, B. Tang, Y. Liu, S. Gao, A. A. Alshehri, I. Shakir, P. O. Agboola, Q. Kong, Q. Wang, D. Ma and X. Sun, *Small*, 2022, **18**, 2106961.
- 176 R. Zhang, Y. Guo, S. Zhang, D. Chen, Y. Zhao, Z. Huang, L. Ma, P. Li, Q. Yang, G. Liang and C. Zhi, *Adv. Energy Mater.*, 2022, **12**, 2103872.
- 177 Z. Ren, Q. Chen, X. An, Q. Liu, L. Xie, J. Zhang, W. Yao, M. S. Hamdy, Q. Kong and X. Sun, *Inorg. Chem.*, 2022, **61**, 12895.
- 178 W. Zhu, X. Zhang, F. Yao, R. Huang, Y. Chen, C. Chen, J. Fei, Y. Chen, Z. Wang and H. Liang, *Angew. Chem., Int. Ed.*, 2023, **62**, e202300390.
- 179 F. Zhou and C. Sun, *Small*, 2022, **18**, 2200436.
- 180 W. Lin, E. Zhou, J. Xie, J. Lin and Y. Wang, *Adv. Funct. Mater.*, 2022, **32**, 2209464.
- 181 R. Zhang, C. Li, H. Cui, Y. Wang, S. Zhang, P. Li, Y. Hou, Y. Guo, G. Liang, Z. Huang, C. Peng and C. Zhi, *Nat. Commun.*, 2023, **14**, 8036.
- 182 X. Lv, J. Ren, Y. Wang, Y. Liu and Z. Yuan, *ACS Sustain. Chem. Eng.*, 2019, **7**, 8993.
- 183 H. Wang, C. Weng and Z. Yuan, *J. Energy Chem.*, 2021, **56**, 470.
- 184 Z. Li, Z. Deng, L. Ouyang, X. Fan, L. Zhang, S. Sun, Q. Liu, A. A. Alshehri, Y. Luo, Q. Kong and X. Sun, *Nano Res.*, 2022, **15**, 8914.



- 185 W. Yu, J. Yu, M. Huang, Y. Wang, Y. Wang, J. Li, H. Liu and W. Zhou, *Energy Environ. Sci.*, 2023, **16**, 2991.
- 186 J. Ren, L. Chen, H. Wang and Z. Yuan, *ACS Appl. Mater. Interfaces*, 2021, **13**, 12106.
- 187 H. Chen, Z. Xu, S. Sun, Y. Luo, Q. Liu, M. S. Hamdy, Z. Feng, X. Sun and Y. Wang, *Inorg. Chem. Front.*, 2022, **9**, 4608.
- 188 J. Ren, L. Chen, Y. Liu and Z. Yuan, *J. Mater. Chem. A*, 2021, **9**, 11370.
- 189 H. Wang, J. Si, T. Zhang, Y. Li, B. Yang, Z. Li, J. Chen, Z. Wen, C. Yuan, L. Lei and Y. Hou, *Appl. Catal., B*, 2020, **270**, 118892.
- 190 X. Lv, X. Liu, L. Gao, Y. Liu and Z. Yuan, *J. Mater. Chem. A*, 2021, **9**, 4026.
- 191 L. Zhang, J. Liang, Y. Wang, T. Mou, Y. Lin, L. Yue, T. Li, Q. Liu, Y. Luo, N. Li, B. Tang, Y. Liu, S. Gao, A. A. Alshehri, X. Guo, D. Ma and X. Sun, *Angew. Chem., Int. Ed.*, 2021, **60**, 25263.
- 192 L. Zhang, Q. Zhou, J. Liang, L. Yue, T. Li, Y. Luo, Q. Liu, N. Li, B. Tang, F. Gong, X. Guo and X. Sun, *Inorg. Chem.*, 2022, **61**, 8096.
- 193 Q. Liu, Y. Lin, L. Yue, J. Liang, L. Zhang, T. Li, Y. Luo, M. Liu, J. You, A. A. Alshehri, Q. Kong and X. Sun, *Nano Res.*, 2022, **15**, 5032.
- 194 J. Ren, Y. Ying, Y. Liu, W. Li and Z. Yuan, *J. Energy Chem.*, 2022, **71**, 619.
- 195 Y. Zhang, Y. Li, K. Shi, Z. Zhu, X. Li, H. Xu and J. Gao, *J. Alloys Compd.*, 2022, **925**, 166680.
- 196 X. Lv, Y. Liu, W. Tian, L. Gao and Z. Yuan, *J. Energy Chem.*, 2020, **50**, 324.
- 197 J. Islam, M. Shareef, H. M. Zayed, X. Qi, F. I. Chowdhury, J. Das, J. Uddin, Y. V. Kaneti, M. U. Khandaker, M. H. Ullah and M. K. Masud, *Energy Storage Mater.*, 2023, **54**, 98.
- 198 Z. Zhao, B. Liu, Y. Shen, T. Wu, X. Zang, Y. Zhao, C. Zhong, F. Ma and W. Hu, *J. Power Sources*, 2021, **510**, 230393.
- 199 S. Schismenos, M. Chalaris and G. Stevens, *Saf. Sci.*, 2021, **140**, 105290.
- 200 W. Tian, J. Ren, X. Lv and Z. Yuan, *Chem. Eng. J.*, 2022, **431**, 133210.
- 201 W. Tian, J. Ren and Z. Yuan, *Appl. Catal., B*, 2022, **317**, 121764.
- 202 Y. Zuo, K. Wang, P. Pei, M. Wei, X. Liu, Y. Xiao and P. Zhang, *Mater. Today Energy*, 2021, **20**, 100692.
- 203 W. Lu, C. Xie, H. Zhang and X. Li, *ChemSusChem*, 2018, **11**, 3996.
- 204 Z. Xu, Q. Fan, Y. Li, J. Wang and P. D. Lund, *Renewable Sustainable Energy Rev.*, 2020, **127**, 109838.
- 205 X. Guo, Z. Zhang, J. Li, N. Luo, G. Chai, T. S. Miller, F. Lai, P. Shearing, D. J. L. Brett, D. Han, Z. Weng, G. He and I. P. Parkin, *ACS Energy Lett.*, 2021, **6**, 395.
- 206 Y. Kim and K. Ryu, *Appl. Surf. Sci.*, 2019, **480**, 912.
- 207 Q. Li, Y. Chen, H. Wang, H. Yu, W. Wei, X. Ji, B. Qu and L. Chen, *Sustainable Energy Fuels*, 2022, **6**, 3501.
- 208 N. Singh and B. R. Goldsmith, *ACS Catal.*, 2020, **10**, 3365.
- 209 Y. Feng, Q. Shi, J. Lin, E. Chai, X. Zhang, Z. Liu, L. Jiao and Y. Wang, *Adv. Mater.*, 2022, **34**, 2207747.

